Journal of Structural Geology

Geometry and kinematics of the Middle to Late Miocene salt tectonics, central Egyptian Red Sea margin

–Manuscript Draft–

Manuscript Number:	SG-D-23-00057R2
Article Type:	Original article
Keywords:	Salt tectonics; Salt walls; Evaporites; Quseir Province; Northern Red Sea
Corresponding Author:	Hemin Koyi Uppsala, SWEDEN
First Author:	Moamen Ali, PhD
Order of Authors:	Moamen Ali, PhD
	Hemin Koyi
	William Bosworth, PhD
	Marco Ligi, PhD
	Philip J. Ball, PhD
	Alessandro Decarlis, PhD
Abstract:	The Red Sea basin includes a thick Middle to Late Miocene evaporitic succession that underwent halokinesis and caused intensive reshaping of the seafloor and the development of salt-tectonic structures. However, the geometry and kinematics of these structures are still poorly understood. This study uses 2D and 3D seismic surveys and well data of the northern Egyptian Red Sea to systematically describe the distribution and morphology of salt structures, discuss their initiation, and construct a kinematic model for their origin. Our results indicate that the massive salt layer developed into five major NW-SE to NNE-SSW trending salt walls, characterized by relatively irregular crests and moderately dipping flanks. In addition, several symmetrical and asymmetrical folds and two categories of normal faults (subsalt and suprasalt) have been recognized. Based on our observations, salt mobilization in the study area started in the Late Miocene, during the precipitation of layered evaporites, and continued until the present day. In the northern Egyptian Red Sea, seismic interpretation indicates that halokinesis was triggered by a combination of thin- and thick-skinned systems, where the latter played a major role. The salt layer was welded during the Quaternary as several sags and grabens developed above the salt diapirs. Thick-skinned physical models are compatible with our observations, supporting the impact of basement faulting on Red Sea diapirism.
Suggested Reviewers:	Neil Mitchell, PhD Professor, The University of Manchester neil.mitchell@manchester.ac.uk
	Ken R. McClay, PhD Professor, University of London ken@gl.rhul.ac.uk
	Christopher A.-L. Jackson, PhD Professor, Imperial College London c.jackson@imperial.ac.uk
	Yossi Mart, PhD Professor, University of Haifa yossimart@gmail.com
	Daniele Colombo, PhD Associate Professor, Saudi Arabian Oil Co daniele.colombo@aramco.com
Response to Reviewers:	Dear Ian,

Geometry and kinematics of the Middle to Late Miocene salt tectonics, central Egyptian Red Sea margin

Moamen Ali[1, 2, 3], Hemin Koyi[4*], William Bosworth[5], Marco Ligi[6], Philip J Ball[7] and Alessandro Decarlis[1,2]

[1] Department of Earth Sciences, Khalifa University of Science and Technology, Abu Dhabi, UAE

[2] R.I.C.H. Center: Research and Innovation on CO_2 and H_2, Khalifa University of Science and Technology, Abu Dhabi, UAE

[3] Department of Geology, Assiut University, Assiut, Egypt

[4] Hans Ramberg Tectonic Laboratory, Department of Earth Sciences, Uppsala University, Sweden

[5] Apache Khalda Corp LDC, 11 Street 281, New Maadi, Cairo, Egypt

[6] Istituto di Scienze Marine, CNR, Via Gobetti 101, 40129, Bologna, Italy

[7] Keele University, Faculty of Natural Sciences, Geography, Geology and the Environment, William Smith Building, Newcastle ST5 5BG, UK

[*] *Email:* hemin.koyi@geo.uu.se

Abstract

The Red Sea basin includes a thick Middle to Late Miocene evaporitic succession that underwent halokinesis and caused intensive reshaping of the seafloor and the development of salt-tectonic structures. However, the geometry and kinematics of these structures are still poorly understood. This study uses 2D and 3D seismic surveys and well data of the northern Egyptian Red Sea to systematically describe the distribution and morphology of salt structures, discuss their initiation, and construct a kinematic model for their origin. Our results indicate that the massive salt layer developed into five major NW-SE to NNE-SSW trending salt walls, characterized by relatively irregular crests and moderately dipping flanks. In addition, several symmetrical and asymmetrical folds and two categories of normal faults (subsalt and suprasalt) have been

recognized. Based on our observations, salt mobilization in the study area started in the Late Miocene, during the precipitation of layered evaporites, and continued until the present day. In the northern Egyptian Red Sea, seismic interpretation indicates that halokinesis was triggered by a combination of thin- and thick-skinned systems, where the latter played a major role. The salt layer was welded during the Quaternary as several sags and grabens developed above the salt diapirs. Thick-skinned physical models are compatible with our observations, supporting the impact of basement faulting on Red Sea diapirism.

Keywords: Salt tectonics, Salt walls, Evaporites, Quseir province, Northern Red Sea

1. Introduction

The Red Sea rifting is a relatively young extensional system. The Nubian and Arabian shields in the conjugate margins have been separating since the Late Oligocene-Early Miocene (e.g. McKenzie et al., 1970; Burke and Dewey, 1973). GPS data show that the rifted margins are diverging at different rates from south to north, as the southern Red Sea is extending about 17 ± 1 mm/yr, while the extension rate in the northern Red Sea is only 7 ± 1 mm/yr (ArRajehi et al., 2010). Initially, the extension direction of the Red Sea was N65°E–S65°W, orthogonal to the rift axis. Subsequently, when the northern plate boundary of Arabia shifted from the Gulf of Suez to the left-lateral Dead Sea transform (~14-12 Ma), the extension direction in the northern Red Sea shifted from orthogonal to oblique, with a general NNE trend parallel to the Dead Sea Transform (Lyberis, 1988; Bosworth et al., 2005; ArRajehi et al., 2010). The transition from a continental to an oceanic crust occurred only in the southern and central sectors of the Red Sea (Bonatti et al., 1984; Bonatti, 1985; Ligi et al., 2012). Evidence for continuous or punctuated seafloor spreading

49 has been found with the recovery during marine surveys of basaltic rocks with mid-ocean ridge
50 (MORB) affinity at different sites along the axis between 17° N and 19° 30' N (Fig. 1a; Girdler
51 and Whitmarsh, 1974; Bonatti, 1985). Based on magnetic anomalies, some authors have estimated
52 an age of 5 Ma for the inception of the oceanic crust in the southern Red Sea (Cochran, 1983;
53 Bonatti, 1985; Schettino et al., 2016, 2019). In the central sector, some axial deeps (Thetis and
54 Nereus) were interpreted as isolated ridge segments and consist of 3 to 1 Ma old oceanic crust
55 (Ligi et al., 2012, 2018).

56 Most of the controversies about the northern Red Sea rifting evolution (Masini et al., 2020;
57 Le Magoarou et al., 2021; Ali et al., 2023) are due to the limited access to good data caused both
58 by industrial disclosure policies and by technical limitations on seismic images imposed by the
59 presence of evaporites. Both rift evolution and the crust's nature are unclear (Sultan et al., 1992;
60 Bosworth et al., 1993, 2020; Colombo et al., 2014; Le Magoarou et al., 2021). Several studies have
61 proposed that the northern Red Sea is underlain by oceanic crust (Girdler and Underwood, 1985;
62 Gaulier et al., 1988; Augustin et al., 2021; El Khrepy et al., 2021). For example, Augustin et al.
63 (2021) built a model for the Red Sea using vertical gravity gradient (VGG) and earthquake and
64 bathymetry data. They suggested that the oceanic crust exists in the entire Red Sea, and the seafloor
65 spreading was initiated at 13.5 and 12.8 Ma in the central and northern Red Sea, respectively.
66 Conversely, other studies suggested that the northern Red Sea is a region of hyperextended,
67 thinned continental crust punctuated by several volcanic deeps distributed along the axis (Cochran,
68 1983; Bonatti, 1985; Bosworth et al., 1993; Cochran, 2005; Mahsoub et al., 2012; Mitchell and
69 Park, 2014; Almalki et al., 2015b; Le Magoarou et al., 2021). Ali et al. (2023) used several
70 geophysical datasets and applied 2D forward modelling to study the nature of the crust in the
71 central part of the northern Red Sea. They investigated a scenario where an exhumed lower

72 continental crust or serpentinized mantle is present. Their results suggested that the best fit between
73 the calculated and predicted gravity and magnetic data was obtained by including a limited mantle
74 exhumation at the rift axis.

75 3D seismic and borehole data are commonly used to analyse the salt structures in
76 sedimentary basins (e.g. Fiduk and Rowan, 2012; Jackson et al., 2015; Rojo and Escalona, 2018).
77 The presence of the Middle to Late Miocene salt layer in the Red Sea represents an important
78 factor in the formation of structural traps, controlling the distribution of reservoirs and source rocks
79 and influencing hydrocarbon migration (Beydoun, 1989; Beydoun and Sikander, 1992; Nilsen et
80 al., 1995; Alsharhan and Salah, 1997). In the last five decades, 14 exploratory boreholes were
81 drilled in Egyptian waters. However, no productive field has been discovered, and the distribution
82 of reservoir and source rocks within the margin is poorly understood (Gordon et al., 2010). In the
83 Saudi Arabian and Yemeni margins, several previous studies focused on detailing the presence of
84 salt bodies (Richter et al., 1991; Heaton et al., 1995; Orszag-Sperber et al., 1998; Mohriak, 2019),
85 salt geometry, and the direction of salt flow (Colombo et al., 2014; Rowan, 2014; Almalki et al.,
86 2015a; Feldens and Mitchell, 2015; Mitchell et al., 2017, 2019, 2021, 2022; Muzaffar et al., 2018;
87 Smith and Santamarina, 2022). The data utilized included 2D seismic profiles, Bouguer gravity
88 anomalies, bathymetry, marine magnetotellurics, gravity gradiometry, and controlled-source
89 electromagnetics (Mart and Ross, 1987; Orszag-Sperber et al., 1998; Mitchell et al., 2010, 2021;
90 Colombo et al., 2014; Rowan, 2014). A controversial issue regarding salt has been the interaction
91 of the salt with the postulated oceanic crust in the Red Sea. High-resolution bathymetry images
92 have shown allochthonous salt masses travelling along the seabed. This model has been used as
93 an analogue for other margins (e.g. Angola and Brazil; Mohriak, 2014; Feldens and Mitchell,
94 2015). Despite these studies, the geometry and kinematics of the Middle to Late Miocene salt

95 structures are still poorly understood partly because none of these previous studies have provided
96 a 3D or temporal understanding of the diapirs along the Egyptian margin. In this study, we use 2D
97 and 3D seismic and borehole data from the central part of the Egyptian Red Sea (offshore Quseir)
98 and cross-section reconstructions to study the initiation and evolution of the salt structures. We
99 construct two–way time (TWT) and isopach maps of the massive salt layer, layered evaporites,
100 and Pliocene-Quaternary sediments and use these to provide a systematic description of the
101 distribution and morphology of salt bodies, intra-salt structures, and their ultimate structural
102 variabilities. We also identify the main basement-involved faults penetrating the base of the salt
103 reflection and those affecting the overburden sediments, constrain the relative age of the salt
104 movement, and determine the kinematic scenario that best fits the observed structural styles.
105
106 **2. Geological setting of the northern Red Sea**
107 The Egyptian margin contains numerous km-scale tilted blocks bounded by major NW-SE
108 trending normal faults generally parallel to the Red Sea rift axis (Fig. 1; e.g. Barakat and Miller,
109 1984; Montenat et al., 1988; Patton et al., 1994). The onshore stratigraphy of the northern Red Sea
110 was described in detail by different studies (Jarrige et al., 1990; Bosworth et al., 1998, 2020; Khalil
111 and McClay, 2009), while the offshore type-succession (Fig. 2) has been studied using the few
112 available commercial well data (Fig. 3; Miller and Barakat, 1988; Bosworth et al., 2020). The
113 offshore geological record of the Egyptian Red Sea is divided into two main tectonostratigraphic
114 sequences (Miller and Barakat, 1988): i) pre-rift, represented by igneous and metamorphic rocks
115 and ii) syn-rift, which is divided into an early rift section assigned to the Nukhul Formation
116 unconformably overlain by a main syn-rift section (Fig. 2). The main syn-rift sequence includes
117 Early to Middle Miocene siliciclastic rocks (Rudeis and Kareem Formations) and Middle to Late

Miocene massive salt layer and layered evaporites (Belayim, South Gharib, and Zeit Formations), followed by Plio-Quaternary clastic rocks (Fig. 2).

During the early Middle Miocene, the Aqaba-Levant transform boundary started accommodating the motion of the Arabian plate, resulting in a sharp change in the extension direction. As a consequence, the marine connection of the Red Sea to the Mediterranean Sea became restricted but not terminated, and the sedimentation in the Red Sea changed from open marine to evaporitic (Hughes and Johnson, 2005; Bosworth et al., 2005; Bosworth, 2015). Several authors suggest that the main evaporite sequence (Belayim, South Gharib, and Zeit Formations) was precipitated during the Middle-Late Miocene (e.g., Orszag-Sperber et al., 1998; Bosworth et al., 2005; Bosworth, 2015). The precipitation of the massive salt layer was associated with an arid period during the Late Serravallian-Tortonian, followed by a wet phase in the Messinian (Griffin, 1999, 2002). The Messinian episode, named the Zeit Wet Phase, was associated with a high rainfall time and deposition of the Zeit Formation and its equivalents (Fig. 2.). This formation is characterized by high clastic content compared to the underlying units. Furthermore, Smith and Santamarina (2022) suggested that the precipitation of thin halite and anhydrite beds within the layered evaporite sequence (Zeit Formation) is related to cyclic yet limited seawater recharge and multi-year drying periods of the Red Sea rifted margin. Ball et al. (2018) observed that salt appears to onlap onto exhumed lower crust or mantle rocks in Zabargad Island and along the Saudi Arabian margin, areas in which exhumation probably occurred at ~15-14 Ma (Fig. 4). Evaporite precipitation seems to be largely synchronous over the entire Red Sea and the Gulf of Suez, and likely occurred during a specific rifting stage corresponding to the transition from necking to hyperextension (Rowan, 2014; Ali et al., 2023). Ali et al. (2023) provided a detailed rift domain model for the northern Red Sea. They interpreted the necking zone close to the shoreline, which

141 probably occurred in the Early Miocene due to the formation of an east-dipping detachment fault.
142 The continental crust thinned significantly from 32 km beneath the onshore Quseir region to 22
143 km below the necking domain. The distal domain formed due to the hyperextension processes is
144 found along the offshore Quseir section and is characterized by the deposition of the Middle to
145 Late Miocene evaporite sequence where the thickness of the continental crust thinned to <10 km
146 (Ali et al., 2023, their figure 10). The evaporitic sequence is intensively affected by salt tectonics,
147 forming salt diapirs and salt walls separated by mini-basins filled by clastic rocks and evaporites
148 (Mart and Ross, 1987; Colombo et al., 2014).

149 At the end of the Miocene, the entire Red Sea basin became subaerially exposed (Bosworth
150 et al., 2005; Mitchell et al., 2017, 2021), and a major unconformity surface formed due to this
151 event, which marks the top of the Zeit Formation and is identifiable in seismic reflection data,
152 known as the S-reflector (Ross and Schlee, 1973; Mitchell et al., 2010). It is characterized by a
153 low frequency and high amplitude seismic reflection resulting from the dramatic increase in
154 velocity from ~2200 to 5000 m/s. This dramatic increase in seismic velocity is due to a thin
155 anhydrite unit at the top of the Miocene evaporite, followed by poorly consolidated Pliocene clastic
156 sediments (Colombo et al., 2014). Seafloor spreading initiation in the southern Red Sea, at ~5 Ma,
157 caused the opening of a connection with the Indian Ocean through the Strait of Bab-el-Mandeb.
158 This event enabled a new marine ingression from the south and determined the end of the evaporite
159 precipitation in the basin (Mart and Hall, 1984; Mart and Ross, 1987).

160 The Middle to Late Miocene evaporite sequence was precipitated due to the evaporation
161 of seawater occasionally entering into the hydrographically semi-isolated Red Sea Basin. It is
162 identified as basinwide marine evaporites, resulting from a combination of hydrological and
163 tectonic circumstances (Warren, 2010). Smith and Santamarina (2022) suggested that the salt

precipitation in the Red Sea was controlled by the recharge rate of the seawater through the Bab-el-Mandeb Strait. The formation of a 1 km thick salt layer resulted from the evaporation of 53 km of Red Sea seawater. On the contrary, Hovland et al. (2015) provided a new model (hydrothermal salt model) where they assumed that the Red Sea's evaporite sequence formed due to the hydrothermal circulation of seawater.

Several previous studies suggested that the Red Sea salt was mobilized dominantly by thin-skinned gravitational failure, with proximal extension and distal contraction (Heaton et al., 1995; Rowan, 2014; Tubbs et al., 2014). On the other hand, the presence of alluvial fans and carbonate platforms parallel to the current coastline is interpreted as the dominant component of nearshore salt movement in the central and southern Red Sea (Smith and Santamarina, 2022). Mart and Ross (1987) postulated that the high thermal gradient, caused by highly attenuated crust and underlying ascending mantle, may have triggered salt diapirs structures. The salt diapirs observed by Mart and Ross (1987) in the northern Red Sea have a NW-SE trend with an average length and width of 30 and 4 km, respectively.

3. Data and methods

2D and 3D seismic surveys and borehole data have been used to study the geometry and kinematics of the Middle to Late Miocene salt structures in the central part of the Egyptian margin (Fig. 3). The 3D seismic survey was acquired by British Gas in 1999 and covers 1600 km^2 offshore Quseir province between 26 and 26° 25' N (Fig. 3; Gordon et al., 2010). It consists of 1729 NW-SE in-lines with a line spacing of 25 m and 4879 NE-SW cross-lines with 12.5 m spacing. Time-migrated seismic data allow imaging up to 7 s TWT. Furthermore, six 2D seismic profiles with a total length of ~471 km were used. The seismic profiles were acquired by Philips and Esso Red

187 Sea between 1975 and 1977 with vertical seismic recording of 6 and 5 s TWT, respectively. Three
188 wells that penetrated the Precambrian basement (granite, granodiorite and gabbro) are used to tie
189 seismic data: Quseir B-1X, Quseir A-1X, and RSO-B 96-1 (Fig. 3). The RSO-B 96-1 was drilled
190 by Esso Red Sea in 1980 reaching a total depth of 4258.08 m from water surface; Quseir B-1X
191 and Quseir A-1X wells were drilled by Philips Red Sea between 1977 and 1978 to a total subsea
192 depth of 4213.86 m and 5038.34 m, respectively.

193 Seismic interpretation procedures accounted for seismic-to-well ties, fault interpretation,
194 and seismo-stratigraphic units picking offshore Quseir, constructing TWT and isopach maps for
195 the salt layer, layered evaporites, and post-evaporitic sediments using the Schlumberger Petrel™
196 software (e.g. Ali et al., 2018, 2020). Six horizons and five seismic sequences (Plio-Quaternary,
197 layered evaporites, transparent evaporites, Pre-salt II, Pre-salt I, and basement) were interpreted
198 picking the upper limit of each formation based on well data, regional continuity, and amplitude
199 of the seismic reflections. The top surface of the Plio-Quaternary sequence and layered evaporites
200 was interpreted for every single crossline and inline with high confidence, using a 3D auto-tracking
201 tool. Concurrently, the interpretation of the other horizons was done manually every 50 crosslines
202 and inlines with some uncertainties. The ages of selected seismic units are taken from previous
203 lithostratigraphic studies of the northern Red Sea (Hughes and Beydoun, 1992; Bosworth et al.,
204 1998; Hughes and Johnson, 2005; Khalil and McClay, 2009). The major phases of salt flow were
205 determined based on identifying growth strata, toplap, onlap, downlap, and truncation surfaces
206 (Figs. 5-13). The RMS amplitude was applied to the 3D seismic cube to delineate the boundary of
207 the salt walls in the time domain. Six time slices have been extracted at TWT values between 1.2
208 and 2.5 s. Depth-converted structural reconstructions were made based on interpreted seismic
209 surveys to estimate the progressive evolution of the salt diapirs. The last 20 km in the southwestern

210 part of the geological model is constructed based on the seismic interpretation in Figure 5 of Ali
211 et al. (2023). Time-to-depth conversions were performed by adopting an average velocity value
212 for each seismic sequence (Table 1; Gaulier et al., 1988; Makris and Rihm, 1991; Rihm et al.,
213 1991; Saleh et al., 2006; Ligi et al., 2018). Due to the difficulty in determining the exact timing of
214 fault movement and displacement amount, the extension and shortening values in the
215 reconstructions have some uncertainties.
216
217 **4. Results**
218 **4.1 Seismic stratigraphy**
219 Six seismic crosslines from the 3D seismic survey and three 2D seismic lines (Figs. 5-13)
220 were interpreted to highlight the main structures (subsalt and suprasalt faults, seismic units, and
221 salt diapirs). Interpreting the top of the basement was challenging due to the thick, overlying
222 evaporite section. However, a continuous high-amplitude seismic reflection in the shallow domain
223 was interpreted as the top of the basement (Fig. 10). Well-control added some confidence to this
224 interpretation, even in the deepest part of the study area. In the time domain, the basement is easily
225 recognizable at a depth of 1 s TWT in the slope area (Fig. 10) to ~4.5 s further offshore with some
226 uncertainties (Fig. 13). The basement is uplifted in the central part of the offshore Quseir, where
227 it is cut by a set of normal faults forming two major structural highs (Figs. 5 and 10). Furthermore,
228 two basement highs reaching the seafloor (Fig. 5) were recognized in the northeastern part.
229 The subsalt sediments are divided into two seismo-stratigraphic units: Pre-salt I and Pre-
230 salt II (Figs. 5 and 8). The Pre-salt I sequence unconformably overlays the basement and is
231 restricted to the deepest parts of the southeastern and central segments of the study area. The Pre-
232 salt I is approximately 0.1-0.7 s thick (150-900 m) and contains flat-lying to sub-horizontal,

moderately layered, high-amplitude reflections (Figs. 5 and 8). The Pre-salt II was unconformably deposited above the crystalline basement in most of the offshore Quseir; however, it is locally found conformably above the Pre-salt I. This sequence is characterized by low to moderate amplitude and moderately to well-layered reflections (Figs. 5-13). The Pre-salt II facies display large thickness variation ranging from 0.15 to 1.5 s TWT (ca. 200-2100 m). Seismic profiles also show that the Pre-salt II was not deposited in the basin flanks, offshore the modern Egyptian coast (Figs. 10-12).

Evaporitic rocks are grouped into two main sequences; seismically "transparent" evaporites (massive salt) overlain by layered evaporites (Figs. 5-13; Izzeldin, 1987; Colombo et al., 2014; Mitchell et al., 2017; Ali et al., 2023). The base and top surfaces of the massive salt layer display strong reflections with high amplitudes, whereas internally, the unit is chaotic with low-amplitude reflectivity. The salt interval is widely distributed in the distal margin but not recorded towards the coast (Figs. 10 and 12). Three main subbasins have been recognized between the main salt structures (Figs. 6 and 10), consisting of thick sedimentary successions of layered evaporites and Plio-Quaternary sediments. These mini-basins are labelled southwestern subbasin (SB1), central subbasin (SB2), and northeastern subbasin (SB3) (Figs. 5 and 6). Northeast of the basement structural highs, the salt sequence becomes thin, characterized by poorly defined layering and low amplitude reflections, and salt structures disappear (Fig. 5).

The layered evaporites unit consists of continuous, moderately to well-stratified seismic reflections with moderate to high amplitude intercalated with continuous and low amplitude reflections (Figs. 5-13). In the western sector of the offshore Quseir, the seismic reflections of the layered evaporites downlap on the salt layer and the basement (Figs. 10-12). In the southwestern mini-basin (SB1), the layered evaporites are characterized by inclined reflections dipping

256 southwest and northeast with moderate thickening towards the southwest (Fig. 12). The central
257 subbasin (SB2) shows slight width variations, ranging from 9 km to 11 km (Figs. 5, 6, 8 and 10).
258 The subsalt faults controlled the deposition of the layered evaporites, as the unit moderately
259 thickens toward the southwest in most of the interpreted seismic profiles (Figs. 5-7 and 9-11),
260 except in the central area where it thickens in the opposite direction (Fig. 8). The layered evaporites
261 are characterized by seismic reflections dipping southwest and northeast within the northeastern
262 subbasin (SB3) and show discordant relationship with the salt diapirs (Figs. 6 and 10). This seismic
263 sequence displays a moderate thickness variation in the SB3, expressed by a small SW thickening
264 in the southeastern sector of the offshore Quseir (Fig. 6) and a SW thinning in the northwestern
265 sector (Fig. 10). The layered evaporites contain several growth seismic sequences, characterized
266 by southwestward shifting depocenters (Figs. 6 and 12). In addition, sedimentary features like
267 angular unconformity, downlap, and truncated toplap closures are recognized in the lower part of
268 the layered evaporite interval (Fig. 11). The top reflection of the layered evaporites is obvious and
269 shows very high amplitude, representing an unconformity surface between the interbedded
270 evaporites and Pliocene sediments (Fig. 5). Several normal faults with small to medium offset cut
271 the upper part of the layered evaporites (Figs. 5-13).
272 The layered evaporites are unconformably overlain by the Plio-Quaternary sequence,
273 representing the youngest sedimentary unit identified in the northern Red Sea. This sequence was
274 deposited over the entire study area, including onshore (Fig. 5; Khalil and McClay, 2002, 2009),
275 and consists of well-stratified, medium to high amplitude seismic reflections. The salt diapirs do
276 not intrude on the Plio-Quaternary sequence (Figs. 5-13). Generally, growth seismic sequences are
277 observed within the basins, showing prominent depocenters that shift towards the southwest (Figs
278 6 and 8). In the southwestern subbasin (SB1), at least three major sedimentary cycles separated by

279 truncation surfaces are observed within the Plio-Quaternary sequence (Fig. 12). Several minor
280 normal faults with steep to moderate dip angle and low offset are recognized within this sequence
281 (Figs. 5-13).

282 **4.2 Well stratigraphy and correlation**

283 Figure 14 displays the correlation of three wells along a NW-SE direction from RSO-B 96-
284 1 in the northwest to Quseir B-1X in the southeast of the study area (Fig. 3). The available well
285 data indicate that the siliciclastic syn-rift sequence corresponds to three formations (Nukhul,
286 Rudeis, and Kareem). The Nukhul Formation is recorded only in RSO-B 96-1 well with a total
287 thickness of ~52 m and mainly includes sandstone. The Rudeis Formation is composed of
288 claystone intercalated with thin sandstone and limestone interbeds. Its thickness varies from ~1685
289 m in the RSO-B 96-1 well to ~1805 m in the Quseir A-1X (Figs. 3 and 14). The Kareem Formation
290 represents the upper part of the pre-salt sequence in the northern Red Sea. It is formed by claystone,
291 siltstone, and sandstone interlayered with thin beds of calcareous limestone and dolostone. The
292 Kareem Formation shows a slight thickness variation between 138 m at Quseir A-1X to 142 m at
293 RSO-B 96-1 (Fig. 14).

294 The evaporite sequence corresponds to three formations: Belayim, South Gharib, and Zeit.
295 The Belayim Formation mainly consists of anhydrite and halite interlayered with dolostone,
296 calcareous limestone, and siltstone. Its thickness varies from 92 to 97 m in the Quseir A-1X and
297 RSO-B 96-1 wells, respectively. The South Gharib Formation represents the main massive salt
298 layer in Quseir offshore and shows a dramatic thickness variation ranging from 245 m at RSO-B
299 96-1 to 3225 m at Quseir B-1X (Fig. 14). It is composed of massive halite intercalated with thin
300 beds of anhydrite. The Zeit Formation includes halite and anhydrite with sandstone, siltstone, and
301 claystone interlayers. The thickness of the Zeit Formation significantly changes between 1115 and

1762 m in the RSO-B 96-1 and Quseir A-1X wells, respectively. However, it is not recorded in Quseir B-1X (Fig. 14). The Plio-Quaternary sequence (Shukheir Formation) is formed by sandstones with thin siltstone and claystone interbeds. Its thickness ranges from 180 m at RSO-B 96-1 to 316 m at Quseir B-1X (Fig. 14).

4.3 Geometry and regional distribution of salt diapirs

Seismic data show that, in the study area, the seismically "transparent" evaporite layer forms five major diapiric walls and three immature diapirs, disappearing toward the northwest (Figs. 5 and 6). The major and more mature salt diapiric walls are labelled D1, D2, D3, D4 and D5 (Figs. 5-11). Most of the salt walls have relatively irregular crests and moderately-dipping flanks. They are NW striking in the southeastern region of the offshore Quseir and NNW to NNE in the northwestern region (Supplementary Video 1). Salt walls are characterized by a slight discordance with the overburden beds and contractional anticlines with uplifted and eroded crests (e.g., Figs. 5 and 6). The geometry of salt walls changes along the strike. The D1 structure has a total length of ~31 km and narrows upward from ~4.3 km at the base to ~1.4 at the neck (Figs. 15 and 16). The height of the wall varies from 0.8 s TWT (~1700 m) to the northwest to 1.2 s TWT (~2500 m) in the southeast (Fig. 15). Salt wall D2 is the longest structure in the offshore Quseir with a total length of approximately 46 km (Figs. 15 and 16). It has an average width of 5 km at the base, and 1.5 km at the crest, and its height increases from 0.6 s TWT (~1250 m) in the northeast to1.2 s TWT (~2500 m) in the central part (Figs. 15 and 16). In the southeastern sector of the offshore Quseir, a subcircular salt body (D3) is observed (Fig. 15). This salt body surrounds a recent volcanic edifice and has an average length and width of about 16 and 6 km, respectively (Figs. 5, 15 and 16; Ali et al., 2022a). Its thickness ranges between 0.3 and 0.8 s TWT (600-1700 m). Salt wall D4 is striking NNW to NNE, is 17 km long and ~2.3 km wide with an average thickness of

about 0.9 s TWT (~1900 m) (Figs. 15 and 16). The seismic data only partly image D5, which shows an average width and thickness of 1.7 and 0.8 s TWT (~1700 m), respectively (Fig. 15).

Figure 13 shows an interpreted 2D seismic section trending SSE-NNW with a total length of approximately 140 km. The seismic profile crosses obliquely (~25°) several salt walls. The interpreted seismic section displays five salt structures, two of which are also present in the central sector of the 3D seismic profiles (as described above, Fig. 13). The other three salt structures (D6, D7, and D8) were recognized in the NNW and SSE sectors of the seismic section. Salt structure (D6) is marked by very strong reflections at its top and base. It has a relatively flat crest and moderately dipping flanks, and an average thickness of about 0.8 s TWT (~1700 m; Fig. 13). Salt wall (D7) is located SSE of RSO B96-1 well, where the seismic section probably marginally cuts the salt structure. It is characterized by an irregular to triangular crest with a height of 0.6 s TWT (~1250 m; Fig. 13). Salt wall (D8) displays continuous high-amplitude reflections parallel to subparallel at its base and top (Fig. 13). The crest of D8 is relatively flat and the flanks are moderately steep (~45°), while the average thickness is about 1.2 s TWT (~2500 m).

4.4 Structural elements

Based on the interpreted seismic data, the main structural elements in the offshore Quseir are normal faults and anticline and syncline folds (Figs. 5-13). Normal faults are classified into subsalt and suprasalt structures. The subsalt faults are rooted in the crystalline basement and cut through the entire subsalt sequence, with some of them displacing the base of the massive salt layer, creating horsts beneath the positions of the major salt diapirs (e.g. Figs. 9-11). The layered evaporites and post-evaporitic deposits appear to be unaffected by faults developed in the subsalt sediments, except for the master faults (Figs. 5, 10 and 20). The low-angle normal fault F1a occurs near the shoreline of the Egyptian margin. It dips to the northeast and displays a large vertical

348 throw offsetting the basement by about 2.8 s TWT (Figs. 10 and 12). The true dip angle changes
349 from ~25° at 1 s TWT to ~12° at 2.5 s (TWT). F1b fault dips to the northeast with a dip angle
350 varying between ~25° at 1.7 s TWT and ~10° at 3.4 s (TWT) and cuts through the basement (Fig.
351 10). F2 is located in the southeastern part of the offshore Quseir and dies out northwestward. The
352 true dip angle decreases from 45° near the seafloor to 15° at the top of the basement (Figs. 5 and
353 17).

354 Normal faults in the suprasalt sequence mainly affect the upper part of the layered
355 evaporites and the Pliocene to recent sequence; however, a few are rooted at the top of the salt
356 layer (Figs. 10 and 11). These faults dip northeast and southwest with moderate to high dip angles
357 (~45°-75°), showing limited throws, usually a few tens of meters (Figs. 5-8). The offset of the
358 suprasalt normal faults increases northwestward, where it may reach 200 m (Figs. 10 and 11).
359 Moreover, the density of the suprasalt faults increases directly above the crests of the salt structures
360 and decreases at the depocenters of the subbasins (Figs. 5-13).

361 Several anticline and syncline folds are imaged in the offshore Quseir (Figs. 5-13). They
362 involve layered evaporites and the Pliocene to recent deposits (Figs. 17b and c). In the southern
363 segment of the study area, symmetrical and asymmetrical synclines, separated by anticlines, are
364 observed. They have moderately inclined limbs and typically trend NW-SE, parallel to the salt
365 walls in this area (Figs. 5, 17b and c). Lengths and amplitudes of the folds vary from about 7 to 45
366 km and 0.4 to 0.7 s TWT (~600-900 m), respectively, and have a wavelength of more than 6 km
367 (Figs. 5 and 17b). The density and complexity of the recognized folds increase toward the
368 northwest, where many of them (>20) were identified (Figs. 8, 10 and 17b). They are symmetric
369 and asymmetric; however, the latter are more common and have gently to moderately inclined
370 limbs. They are generally smaller than the structures in the southern sector of the offshore Quseir,

371 where they reach an average length of about 5 km and an average amplitude and wavelength of
372 0.4 s TWT (600 m) and 5 km, respectively (Figs. 8, 10 and 17b). The folds typically trend from
373 NNE-SSW to NE-SW, subparallel to the salt walls in this region (Fig. 17b).

374 **4.5 TWT structural and isopach maps**

375 TWT maps of the top of the Plio-Quaternary and layered evaporites sequences are shown
376 in figures 17a and 17b, respectively. The TWT structural map of the top of the Plio-Quaternary
377 sequence shows that the maximum depths are observed in the eastern and northeastern sectors,
378 while the minimum values are distributed in the western and northwestern regions (Fig. 17a).
379 Seafloor depth, expressed as TWT, ranges from 0.55 to 0.65 s (~425-500 m bsl) towards the
380 present shoreline and from -1.2 to -1.35 s (~930-1050 m bsl) in the deepest sectors of the offshore
381 Quseir (Fig. 17a). The time domain structural map of the layered evaporites exhibits a different
382 pattern (Fig. 17b). In fact, the top of this sequence reaches the highest values, ranging from 2.0 to
383 2.1 s TWT (~2000-2100 m bsl), in the northwestern region of the offshore Quseir. In contrast, the
384 shallow areas, controlled by the distribution of the underlying salt walls, form NW-SE elongated
385 patterns. These regions display TWT values ranging from 0.9 to 1.1 s (900-1100 m bsl) and are
386 separated by embayments reaching depths between 1.3 and 1.65 s (~1300-1650 m bsl; Fig. 17b).
387 The structural setting of the offshore Quseir is mainly controlled by two major sets of extensional
388 faults trending NW-SE to NNW-SSE and NE-SW to ENE-WSW (Fig. 17). Most of the NW-SE to
389 NNW-SSE normal faults dip seaward (NE to ENE) and their lengths along strike vary from 1 to
390 11 km. The NE-SW to ENE-WSW set mainly dips toward the SE, and their lengths along strike
391 range between 1 and 7 km (Fig. 17).

392 The TWT maps of the top and base of the massive salt sequence are shown in Figures 18a
393 and 18b, respectively. The map of the salt-layer top shows that the minimum depths are distributed

394 along the crests of the salt walls, ranging from 1.0 to 1.3 s TWT (~1000-1300 m). In contrast, the
395 deepest areas are recorded in the subbasins formed between the salt structures and in the western
396 and northwestern regions of the study area, parallel to the present shoreline (Fig. 18a). The depths
397 in these regions vary between about 2.1 and 3.0 s TWT (~2450-3700 m bsl). The fault density
398 sharply decreases toward the top of the salt unit, where only a few normal structures, trending
399 NNE-SSW, NW-SE and E-W, were recognized in the eastern sector of the offshore Quseir. They
400 are located around the volcanic edifice mentioned above and display lengths varying from 1.5 to
401 9 km (Fig. 18a). The minimum depths of the salt base (Fig. 18b) are found beneath the salt walls
402 with values ranging from 1.6 to 2.1 s TWT (~2650-3800 m bsl), while the maximum depths are in
403 the regions between the salt structures, which vary from 2.2 to 3.1 s TWT (~2650-3900 m bsl).
404 The fault interpretation below the massive salt sequence is challenging. However, several major
405 normal faults, all striking NW-SE parallel to the salt walls and lengths varying between 10 and 15
406 km, have been recognized to offset the salt base. The subsalt normal faults dip NE and SW and
407 define a few major highs (Fig. 18b).

408 Three isopach maps have been made for the Plio-Quaternary, layered evaporites and salt
409 layer to analyze their thickness distribution (Fig. 19). The Plio-Quaternary sequence has a
410 maximum thickness of over 1.2 s TWT (~1200 m), reached in the northwestern part of the offshore
411 Quseir. This thickness decreases dramatically eastward and southeastward, in correspondence with
412 the crests of the salt structures, with a TWT value from 0.1 to 0.2 s (~100-200 m). The thickness
413 of the sediments increases in the regions between the salt structures with an average value of about
414 0.5 s TWT (~500 m; Fig. 19a). The isopach map of the layered evaporites shows the highest and
415 abrupt thickness variations, approaching the minimum thickness in the areas directly above the
416 salt walls and stock (0.1 s TWT; 175 m). The thickness of the layered evaporites increases

417 dramatically in the subbasins located between the salt structures, where it ranges from 0.8 to 1.5 s
418 TWT (1400-2600 m; Fig. 19b). The isopach map of the massive salt sequence exhibits an opposite
419 trend as the maximum thicknesses are located at the salt walls, with values ranging from 0.6 to 1.2
420 s TWT (~1250-2500 m). The minimum values, ranging between 0 and 0.1 s TWT (~0-400 m), are
421 found in the welded basins (Fig. 19c).
422
423 **5. Discussion**
424 **5.1 Structural evolution**
425 Based on the interpretation of seismic sections, a four-stage tectonostratigraphic model for
426 the structural evolution of the southern part of offshore Quseir is proposed. The model begins with
427 the deposition of the pre-salt sediments, followed by the precipitation of the salt layer. This model
428 explores salt movement up to the present day (Fig. 20), emphasizes the distribution of salt
429 formations (the salt layer and layered evaporites), and investigates the timing of salt movement,
430 shifting of depocenters, and welding/salt depletion at specific locations.
431 *Stage 1 (Middle-Late Miocene)*
432 Before deposition of the Middle Miocene salt layer, a structural low bounded by two low-
433 angle normal faults (F1 and F2) was present in the area. A Cretaceous-Eocene pre-rift and Late
434 Oligocene-Middle Miocene syn-rift successions may have been present at the base of this basin,
435 although pre-rift strata were never confirmed by drilling data (Bosworth et al., 2020). Nevertheless,
436 it must be stressed that wells were usually drilled on structural highs, where such successions were
437 thin, not deposited, or eroded. These successions have been combined in one seismo-stratigraphic
438 unit labeled pre-salt sequence (Fig. 20d). The pre-salt sequence overlies the crystalline basement
439 unconformably and shows large lateral variations; its thickness decreases northeastward from

about 2200 m in the depocenter to approximately 1300 m in the northeastern end of the graben (Fig. 20d). However, the main massive salt layer was precipitated in the Middle-Late Miocene during the hyperextension stage of the northern Red Sea and was restricted to the necking and distal domains, but is absent in the proximal domain (Ali et al., 2023, their figures 5 and 10). Estimating the initial thickness of the salt remains challenging due to the lack of seismic and well data, the base of salt layer may not be flat (i.e., initial salt is thicker in grabens and half grabens), and salt flows in and out of the study area. However, based on the interpreted seismic sections and forward modeling, a crude estimation is made of approximately 1500 m of mobile salt being precipitated in the deepest part of the basin (*see* Ali et al., 2023). Locally, in the southeastern part of the offshore Quseir, only a few hundred meters of salt was precipitated (Fig. 20d). Seawards, beyond these basement highs, the current thickness of the salt layer is ~1200 m. Although the lower salt layer is generally seismically transparent (Figs. 5-13), it includes few high-amplitude reflections. These reflections are probably related to non-evaporitic lithologies (e.g. carbonate interbeds) or to thin anhydrite layers dragged by salt flow, similar to what is observed within the salt structures (Figs. 5, 9 and 10). This interpretation is compatible with the available boreholes where the salt layer consists of halite intercalated with thin beds of anhydrite and with observations reported in the previous literature (Fig. 14; Izzeldin, 1987; Orszag-Sperber et al., 1998; Koyi, 2001; Mitchell et al., 2017). Some of the basement faults are assumed to be obscured by diapirs. However, several reactivated basement faults are observed in the seismic sections (Figs. 9-11), forming structural highs beneath the salt layer and the diapirs (Figs. 10 and 20d).

The precipitation of the salt layer was followed by the deposition of the layered evaporites in the Late Miocene (Figs. 4 and 14). Growth seismic sequences and moderate to large thickness variation are observed in these sediments, which indicate a Late Miocene synhalokinetic

463 deposition (Figs. 12 and 20d). During this period, several NW-SE basement faults were active.
464 They resulted in the formation of depressions where layered evaporites deposited, causing
465 differential loading and withdrawal of the underlying salt (Fig. 20d). These observations indicate
466 that the northern Red Sea underwent thick-skinned extension during the Middle Miocene.
467 Movement along and reactivation of basement faults and subsequent and accompanying
468 differential loading triggered salt movement (Koyi, 1991; Vendeville and Jackson, 1992a, 1992b;
469 Koyi et al., 1993a; Jackson and Vendeville, 1994). Variations in the thickness of the layered
470 evaporites and the structures displayed between the salt diapirs may indicate the passive stage of
471 diapiric growth with the beginning of the deposition of the layered evaporites. The continuous
472 movement of the major reactivated basement faults and salt movement caused the formation of
473 several suprasalt normal faults with NW to NNW dominant trend, parallel to sub-parallel to strike
474 of the salt structures (Figs. 17b and 20d). The downlaps of the layered evaporite reflections near
475 the present Egyptian shoreline are probably generated by hanging wall subsidence above a low-
476 angle growth fault (Fa1, Fig. 12).

477 *Stage 2 (Early Pliocene)*

478 The Pliocene-Quaternary sequence is characterized by several sedimentary cycles (Figs.
479 10 and 12), which are divided into two main stages for simplicity. The Early Pliocene siliciclastic
480 deposits were unconformably deposited above the layered evaporites, which were mobile (Fig.
481 14). The resulting erosional surface (labelled S-reflector) is sharp and evident at different locations
482 in all the seismic sections (Figs. 5-13). Erosion of the layered evaporites, attributed to an abrupt
483 fall of the Red Sea level in the latest Miocene or the earliest Pliocene (Mitchell et al., 2021), was
484 probably due either to subaerial exposure (Colombo et al., 2014) or to the effect of waves in the
485 shallow marine environment (Mitchell et al., 2017). The S-reflector is strongly reflective and

continuous above the salt diapirs and anticlines of the layered evaporite sequence. In contrast, this erosive surface is vague in the basins, where Pliocene reflections seem to be conformable with those of layered evaporites. It is commonly regarded as a correlative conformity (Cartwright et al., 1993; Li and Schieber, 2022), indicative of depositional continuity (Figs. 5-13). This observation suggests that the top surface of the layered evaporites was probably not flat but displayed relief due to salt movement, and some parts of the surface remained submerged even during the drawdown of the Red Sea level.

The large thickness variation in the Pliocene sequence and its discordant relationship with the layered evaporites are interpreted to indicate that halokinesis was active during this period, creating mini-basins flanked by salt diapirs (Fig. 20c). Several growth seismic sequences were observed within the mini-basins, onlapping the uplifted layered evaporites. Furthermore, toward the shoreline, indication of depocenters migration is evident, indicating salt basinward flow (Figs. 5-12). Preexisting suprasalt faults remained active while new ones were formed due to the continuous salt evacuation and probably due to continued movement along the basement faults. Movement along the subsalt and suprasalt faults and the differential loading in stages 1 and 2 were responsible for the evacuation and expulsion of most of the salt layer into the layered evaporites and the development of the major salt structures offshore Quseir. The basement highs northeast of the master faults within the basin (F2 and F3) may have hampered seaward salt flow (Figs. 5 and 20c).

Stage 3 (Plio-Pleistocene)

Continuous evacuation of the remaining salt during the Plio-Pleistocene caused subsidence between the major salt structures. New siliciclastic sediments were deposited unconformably above the Early Pliocene sequence, indicating erosional surfaces between two sedimentary cycles

509 (Figs. 6, 8, 10, 12 and 20b). Movement of the underlying salt caused the migration of depocenters
510 southwestward. Furthermore, during this stage, most of the remaining mobile salt in the
511 southwestern region of the offshore Quseir was depleted (Figs. 5-11 and 20b). In contrast, a
512 significant amount of salt, with an average thickness of 500 m, remained surrounding the basement
513 highs in the southeastern sector of the study area (Fig. 20b). Most of the suprasalt faults die out
514 before cutting the seafloor. However, in the northwestern and southeastern regions of the offshore
515 Quseir, several suprasalt faults have been recognized offsetting the seafloor with throws ranging
516 from a few tens of metres to 200 m (Figs. 5, 10, 17a and 20b).

517 *Stage 4 (Volcanic Eruption)*

518 The Quaternary period witnessed a magmatic event in the northern Red Sea as several
519 volcanic edifices have been recognized from geophysical data (Cochran et al., 1986; Ali et al.,
520 2022a, 2022b). The two basement highs recognized in the southeastern region of the Quseir, near
521 the Brothers Islands, were identified as volcanic sites (Ali et al., 2022a). The magmatic supply
522 followed a generalized crustal thinning stage and probably erupted through major fault zones (F2
523 and F3). The Plio-Quaternary sequence shows significant thinning toward the salt diapirs in some
524 segments of the study area, suggesting continued salt movement and growth of salt structures
525 (Figs. 5, 6 and 20a). Moreover, most of the salt structures offshore Quseir experienced minor sag
526 or diapiric falls related to the continuous extension in the Red Sea, which is still an active rift (e.g.,
527 Cochran and Martinez, 1988; Bosworth et al., 2005). The recorded seismicity in the northern Red
528 Sea indicates a large number of earthquakes, which are characterized by low to moderate
529 magnitudes (Al-Ahmadi et al., 2014; Bosworth et al., 2020). The number of seismic events and
530 those of the larger earthquakes gradually increase northward, reaching their maximum at the Sinai
531 triple junction (Bosworth et al., 2020, their figure 9.3). Based on the global Centroid Moment

532 Tensor (CMT) catalogue, the focal mechanisms of the earthquakes, as expected, are predominantly
533 normal dip-slip with strikes in the NNW-SSE and NW-SE directions, parallel to the rift orientation
534 of the Red Sea (Badawy et al., 2008; Abdel-aal and Yagi, 2017).

535 **5.2 Thick-skinned versus thin-skinned extension**

536 Several key features have been observed in the seismic data to support thick-skinned
537 extension as a dominant mechanism for salt mobilization offshore Quseir (Figs. 10 and 20). Thick-
538 skinned extension accompanied by syn-kinematic sedimentation (which has caused differential
539 loading) are likely to have triggered salt movement (Fig. 20). The seismic data used in this study
540 do not provide any evidence to support a progradational loading system or the existence of a
541 sedimentary wedge. The following arguments are used to support the thick-skinned extension:

542 1. Existence of reactivated basement normal faults. Several subsalt faults were recognized on
543 the seismic sections. These faults penetrated the base of the salt sequence and are
544 interpreted to have caused asymmetric sedimentation and differential loading on the
545 underlying salt layer (Figs. 9-11 and 20).
546 2. Large thickness variations in the layered evaporites and Plio-Quaternary deposits (across
547 basement faults). This thickness variation could be related to displacements of basement
548 faults or/and salt withdrawal. The maximum thickness of the overburden is found directly
549 above the hanging wall of the subsalt faults (e.g. Figs. 5 and 9).
550 3. Significant topography at the base of the salt sequence. The seismic sections display large
551 changes in the topography of the base salt, especially across the major subsalt faults (F1
552 and F2; Figs. 5, 10 and 12). Subsalt topography, likely generated by movement along
553 basement (subsalt) faults, played an important role in triggering salt movement and
554 probably controlled the spatial distribution of salt structures.

4. Trend of salt walls. Several salt walls are parallel to and grow above the main structural/fault trend of the Red Sea (NW-SE) (Figs. 10 and 18).
5. The existence of gravity gliding and suprasalt faults. Subsalt faults contributed to a change in the slope of the northern Red Sea margin dipping towards the ENE. This has caused extension and gliding of the overburden basinwards above the salt, resulting in the formation of many suprasalt faults. Most of these faults trend NW-SE and are located above and close to the diapir crests (Figs. 5-13).
6. Diapir fall or sag. Suprasalt faults were observed above the crests of the salt structures, indicating continued extension of the area and diapiric fall. It is assumed that the feeding salt layer is depleted and welds formed below mini-basins (e.g. Fig. 5).

Seismic observations indicate that most of the basement faults in the central part of offshore Quseir die out within the salt layer or cannot be traced in the cover units, indicating a decoupled system (e.g. Figs. 6 and 7). However, some major subsalt faults penetrated the salt layer and the overburden, suggesting a coupled system in the eastern and western sectors of the offshore Quseir (Figs. 5, 10 and 11). It is generally thought that the basement will be stretched and faulted in a rifted margin that has undergone crustal extension. Such deformation will directly affect any salt layer resting on this basement. This is corroborated by several physical experiments (Koyi et al., 1993a, 1993b; Withjack and Callaway, 2000; Dooley et al., 2004, 2017; Burliga et al., 2012; Dooley and Hudec, 2017). The salt layer in the Red Sea was precipitated above a faulted basement, which strongly impacted salt flow and sediment deposition. Therefore, it is both likely and expected that salt mobilization was within the framework of thick-skinned tectonics. Salt movement began with the precipitation of the layered evaporites during Late Miocene and continued until Pleistocene, creating several salt walls in the NW-SE to NNW-SSE directions.

578 Although, the interpreted salt structures do not reach the seafloor, their growth must have
579 continued after the deposition of the S-reflector, which is bent above the salt diapirs. The massive
580 salt layer was probably depleted, or the extension rate was greater than the salt supply to the diapirs
581 during the Pleistocene, as several local sag basins and grabens have been recognized above the salt
582 diapirs. They were probably generated due to the salt fall during continued extension along the
583 margin (Figs. 5-11). The seafloor of the study area is irregular, showing changes in bathymetry,
584 indicating that these areas are currently tectonically (and probably, halokinetically) active. Salt
585 movement ceased in some parts of the central region of the Red Sea earlier at the Miocene-Pliocene
586 boundary, implying that salt expulsion was heterogeneous (Mitchell et al., 2022).
587 Rowan (2014) and Tubbs et al. (2014) suggested that the Middle-Late Miocene salt layer
588 was dominantly deformed by thin-skinned gravitational failure, while Smith and Santamarina
589 (2022) proposed that carbonate platforms and alluvial sediment fans drive salt withdrawal. Based
590 on the observations above, we think that thick-skinned extension strongly contributed to salt
591 mobilization and continued movement in the northern Red Sea. However, the presence of gravity
592 gliding, suprasalt faults, ramp syncline basins, and diapir sag show that the thick-skinned extension
593 induced thin-skinned extension offshore Quseir. The thin-skinned extension in offshore Quseir is
594 not considered to be regional; the main basement faults compartmentalize the area into sub-basins
595 where thin-skinned extension occurs locally (Fig. 10). In addition, although there is lateral
596 movement of the layered evaporites and Plio-Quaternary sequence, some of the diapirs remain
597 "resting" above basement horsts influenced by two main basement faults on both sides of the
598 diapirs. Figures 9 and 10 display a good example of salt wall D4, formed above a horst where salt
599 has moved up-dip to the low-pressure zones in the footwall of the subsalt faults. In other words,
600 diapirs feed from both sides of the horst and stay above the basement faults. In an extensional

tectonic system where basement faults dominate, it is likely that the movement of these faults does influence salt diapirism, both as triggers and/or affects the continued evolution of salt structures. Furthermore, it is thick-skinned extension does not exclude thin-skinned extension happening locally in areas between the major basement faults.

5.3 Comparison with physical models

Several examples for salt structures triggered by basement faults are reported by Ford and Vergés (2021) in the Pyrenees margin, in the Danish Basin (e.g. Koyi and Petersen, 1993; Hansen et al., 2021) and the Nordkapp Basin in the Barents Sea (e.g. Koyi et al., 1993b; Rojo et al., 2019). Many studies have described the impact of the basement faults on salt mobilization by using scaled analogue models (e.g. Koyi and Petersen, 1993; Koyi et al., 1993a; Nilsen et al., 1995; Rojo et al., 2020). Seismic observations in the study area are consistent with the results from physical models by Koyi and Petersen (1993; their Figure 5) and Koyi et al. (1993a; their Figures 5 and 6) simulating the effect of basement faults on diapirs. The results from these analogue models can be used to suggest that the basement faults in the northern Red Sea strongly influence the movement of the Middle-Late Miocene salt layer and trigger the growth of salt structures. Most of the interpreted seismic sections indicate that basement faults formed half-grabens overlain by thick overburden units, causing differential loading on the salt layer. The salt moved up-dip to the low-pressure zones in the footwall and up-dip along the uplifted part of the rotated hanging walls (e.g. Figs. 5 and 11). The seismic interpretation suggests that most of the salt walls in offshore Quseir are associated with basement-involved faults (Figs. 5-13). Sandbox model results by Koyi et al. (1993a; their Figure 6) display that salt structures triggered by subsalt faults are not necessarily located directly above these faults. Based on the results from physical models by Withjack et al. (1990), Koyi et al. (1993a) and others, the location of the resulting salt structures is strongly

associated with the overburden deformation due to the basement-involved faulting. They suggested that the basement faults stretched the overburden and created the space through which the salt layer could flow up-dip. Our seismic observations are strongly consistent with this suggestion, as all the salt diapirs offshore Quseir are found below weak zones of the layered evaporites and the Plio-Quaternary sequence. This is also the case for salt wall D3, which is not associated with basement faults (Figs. 5 and 6).

In the southeastern part of the offshore Quseir, a few pillows have been recognized on the uplifted sector of the rotated hanging walls of basement faults. These pillows are immature and smaller compared to the major salt diapirs (D1-D5), located directly above the tip of the basement faults. These observations are compatible with the results of a physical model by Koyi et al. (1993a; their Model 3, Figure 5b). They suggested that, along the fault, salt flows faster due to the higher loading. However, part of the salt in the half-graben is displaced along the tilted hanging wall, where it may form a pillow or an immature salt structure (Figs. 5 and 6).

Furthermore, the seismic data show several ramp-syncline basins (RSBs) characterized by asymmetric and landward depocenter migration. The kinematics and stratigraphic architecture of these structures have been documented in both analogue models (McClay and Scott, 1991; McClay, 1996; Dooley et al., 2017; M. Pichel et al., 2019) and numerical models (Pichel et al., 2018). Model results show two types of RSBs: extensional/classic and salt-detached RSBs. We have used model results to identify extensional and salt-detached RSBs offshore Quseir. The classic RSBs are found on the hanging wall of the F1 master fault (Figs. 10 and 12) and display asymmetric depocentres with basinward-dipping axial trace. However, the geometry and the axial trace of the observed extensional RSBs are strongly compatible with the modeled RSBs by McClay (1996), some components are probably salt-related (Fig. 10). The salt-detached RSBs were

recognized in the SB2 and SB3 between the major salt structures (i.e., between D4 and D2 salt diapirs; Figs. 9 and 10), their geometry and axial trace are similar to the modeled salt-detached RSBs by Pichel et al. (2018). The Plio-Quaternary unit translates above the Middle-Late Miocene evaporite sequence. Like the extensional RSBs, the salt-detached RSBs show a basinward-dipping axial trace with landward-shifting depocenters displaying extension-related components (Figs. 9 and 10). The surface boundaries of both RSBs are diachronous, and they have onlap, baselap and toplap terminations. The RSBs have been documented by Rowan (2014) above the hanging wall of basement faults in the Saudi Arabian margin.

6. Conclusions

Interpretation of two-dimensional and three-dimensional seismic surveys and borehole data support the presence of five major salt walls (D1-D5) and several immature salt structures in the central part of the Egyptian Red Sea rifted margin. The salt walls trend from NW-SE to NNE-SSW and have been interpreted to be associated with basement faults. They show relatively irregular crests and moderately-dipping flanks with an average width of 5 km at the base and 1.5 km at their crest. Salt structures exhibit variable amplitudes between 0.6 and 1.2 s TWT (~1250-2500 m). Salt wall D2 is the longest salt structure, with a total length of approximately 46 km. Salt structures are associated with overburden faults and folds. Our observations support a decoupled system in the offshore Quseir. However, in the eastern and western parts of the study area, the existence of major subsalt faults penetrating the overburden suggests that the stretching overburden was coupled to the subsalt strata and basement.

This study demonstrates that thick-skinned extension was the main driver for salt mobilization in the offshore Quseir. However, locally, the thick-skinned extension resulted in

minor thin-skinned extension, where subsalt deformation is decoupled from that in the overburden. Growth seismic sequences, large thickness variations, and diapiric contacts are observed in the layered evaporites, suggesting that the study area underwent thick-skinned extension during the Late Miocene, i.e., extension affected the continental crust. Furthermore, the presence of suprasalt faults, SW-shifting depocenters, and thickness variation in the Plio-Quaternary sediments indicate that thick-skinned extension continues in offshore Quseir. Moreover, in the central part of the northern Red Sea, the massive salt layer was probably depleted during the Quaternary and the salt walls experienced diapiric fall due to the continuous extension. A comparison between seismic observations and the results from several physical models investigating the influence of basement faulting on salt mobilization supports our interpretation that the basement faults offshore Quseir had a significant impact on the movement of the salt layer and triggered the growth of salt structures.

Acknowledgements

The seismic data were provided courtesy of BG Egypt (now Royal Dutch Shell) and images are published with the permission of South Valley Egyptian Petroleum Holding Company (Ganope). We are grateful to these organizations for providing the data, and approval to publish the paper. We would like to thank Webster Mohriak, Mark Rowan, and an anonymous reviewer for their valuable comments and constructive modifications that greatly enhanced the manuscript.

693

694

695 **References**

696 Abdel-aal, A.K., Yagi, Y., 2017. Earthquake source characterization, moment tensor solutions,
697 and stress field of small-moderate earthquakes occurred in the northern Red Sea Triple
698 Junction. Geosciences Journal 21, 235–251.

699 Al-Ahmadi, K., Al-Amri, A., See, L., 2014. A spatial statistical analysis of the occurrence of
700 earthquakes along the Red Sea floor spreading: clusters of seismicity. Arabian Journal of
701 Geosciences 7, 2893–2904.

702 Ali, M., Abdelhady, A., Abdelmaksoud, A., Darwish, M., Essa, M.A., 2020. 3D static modeling
703 and petrographic aspects of the Albian/Cenomanian Reservoir, Komombo Basin, Upper
704 Egypt. Natural Resources Research 29, 1259–1281.

705 Ali, M., Darwish, M., Essa, M.A., Abdelhady, A., 2018. 2D seismic interpretation and
706 characterization of the Hauterivian–Early Barremian source rock in Al Baraka oil field,
707 Komombo Basin, Upper Egypt. Journal of African Earth Sciences 139, 113–119.

708 Ali, M., Decarlis, A., Ligi, M., Ball, P., Bosworth, W., Ceriani, A., 2023. Red Sea rifting in central
709 Egypt: constraints from the offshore Quseir province. Journal of the Geological Society 180,
710 jgs2022-105. https://doi.org/https://doi.org/10.1144/jgs2022-105

711 Ali, M., Ligi, M., Ceriani, A., Bouchaala, F., Bosworth, W., Decarlis, A., 2022a. Geophysical
712 evidence for magmatism southwest of the Brothers Islands, Northern Red Sea (offshore
713 Quseir, Egypt). Tectonics 41, e2022TC007228.

714 Ali, M., Ligi, M., Ceriani, A., Bouchaala, F., Bosworth, W., Decarlis, A., 2022b. Birth of a large
715 Quaternary volcanic edifice southwest of the Brothers Islets, Northern Red Sea, Egyptian

716 Margin. Working Group on Mediterranean Ophiolites Conference, Abstracts. Ofioliti, Italy,
717 1.
718 Almalki, K.A., Ailleres, L., Betts, P.G., Bantan, R.A., 2015a. Evidence for and relationship
719 between recent distributed extension and halokinesis in the Farasan Islands, southern Red
720 Sea, Saudi Arabia. Arabian Journal of Geosciences 8, 8753–8766.
721 Almalki, K.A., Betts, P.G., Ailleres, L., 2015b. The Red Sea–50 years of geological and
722 geophysical research. Earth-Science Reviews 147, 109–140.
723 Alsharhan, A.S., Salah, M.G., 1997. A common source rock for Egyptian and Saudi hydrocarbons
724 in the Red Sea. AAPG Bulletin 81, 1640–1659.
725 ArRajehi, A., McClusky, S., Reilinger, R., Daoud, M., Alchalbi, A., Ergintav, S., Gomez, F.,
726 Sholan, J., Bou- Rabee, F., Ogubazghi, G., 2010. Geodetic constraints on present- day
727 motion of the Arabian Plate: Implications for Red Sea and Gulf of Aden rifting. Tectonics 29.
728 Augustin, N., Van der Zwan, F.M., Devey, C.W., Brandsdóttir, B., 2021. 13 million years of
729 seafloor spreading throughout the Red Sea Basin. Nature Communications 12, 1–10.
730 Badawy, A., Mohamed, A.M.S., Abu-Ali, N., 2008. Seismological and GPS constraints on Sinai
731 sub-plate motion along the Suez rift. Studia Geophysica et Geodaetica 52, 397.
732 Ball, P.J., Stockli, D.F., Robbins, S., Tugend, J., Masini, E., 2018. Northern Red Sea: Unravelling
733 the tectono-thermal evolution of a hyper-extended rift system. La Réunion Des Sciences de
734 La Terre, Abstract 245.
735 Beydoun, Z.R., 1989. The hydrocarbon prospects of the Red Sea- Gulf of Aden: a review. Journal
736 of Petroleum Geology 12, 125–144.
737 Beydoun, Z.R., Sikander, A.H., 1992. The Red Sea—Gulf of Aden: re-assessment of hydrocarbon
738 potential. Marine and Petroleum Geology 9, 474–485.

739 Bonatti, E., 1985. Punctiform initiation of seafloor spreading in the Red Sea during transition from
740 a continental to an oceanic rift. Nature 316, 33–37.
741 Bonatti, E., Colantoni, P., Dellavedova, B., Taviani, M., 1984. Geology of the red-sea transitional
742 region (22-degrees-n-25-degrees-n). Oceanologica Acta 7, 385–398.
743 Bosworth, W., 2015. Geological evolution of the Red Sea: historical background, review, and
744 synthesis. The Red Sea. Springer, 45–78.
745 Bosworth, W., Crevello, P., Winn, R.D., Steinmetz, J., 1998. Structure, sedimentation, and basin
746 dynamics during rifting of the Gulf of Suez and north-western Red Sea. Sedimentation and
747 Tectonics in Rift Basins Red Sea:-Gulf of Aden. Springer, 77–96.
748 Bosworth, W., Huchon, P., McClay, K., 2005. The red sea and gulf of aden basins. Journal of
749 African Earth Sciences 43, 334–378.
750 Bosworth, W., Khalil, S.M., Ligi, M., Stockli, D.F., McClay, K.R., 2020. Geology of Egypt: The
751 Northern Red Sea. The Geology of Egypt. Springer, 343–374.
752 Bosworth, W., Montagna, P., Pons-Branchu, E., Rasul, N., Taviani, M., 2017. Seismic hazards
753 implications of uplifted Pleistocene coral terraces in the Gulf of Aqaba. Scientific Reports 7,
754 1–13.
755 Bosworth, W., Sultan, M., Stern, R.J., Arvidson, R.E., Shore, P., Becker, R., 1993. Nature of the
756 Red Sea crust: A controversy revisited: Comment and Reply. Geology 21, 574–576.
757 Burke, K., Dewey, J.F., 1973. Plume-generated triple junctions: key indicators in applying plate
758 tectonics to old rocks. The Journal of Geology 81, 406–433.
759 Burliga, S., Koyi, H.A., Chemia, Z., 2012. Analogue and numerical modelling of salt supply to a
760 diapiric structure rising above an active basement fault. Geological Society, London, Special
761 Publications 363, 395–408.

762 Cartwright, J.A., Haddock, R.C., Pinheiro, L.M., 1993. The lateral extent of sequence boundaries.
763 Geological Society, London, Special Publications 71, 15–34.
764 Cochran, J.R., 2005. Northern Red Sea: Nucleation of an oceanic spreading center within a
765 continental rift. Geochemistry, Geophysics, Geosystems 6.
766 Cochran, J.R., 1983. A model for development of Red Sea. Aapg Bulletin 67, 41–69.
767 Cochran, J.R., Martinez, F., 1988. Evidence from the northern Red Sea on the transition from
768 continental to oceanic rifting. Tectonophysics 153, 25–53.
769 Cochran, J.R., Martinez, F., Steckler, M.S., Hobart, M.A., 1986. Conrad Deep: a new northern
770 Red Sea deep: origin and implications for continental rifting. Earth and Planetary Science
771 Letters 78, 18–32.
772 Colombo, D., McNeice, G., Raterman, N., Zinger, M., Rovetta, D., Sandoval Curiel, E., 2014.
773 Exploration beyond seismic: The role of electromagnetics and gravity gradiometry in deep
774 water subsalt plays of the Red Sea. Interpretation 2, SH33–SH53.
775 Dooley, T.P., Hudec, M.R., 2017. The effects of base-salt relief on salt flow and suprasalt
776 deformation patterns—Part 2: Application to the eastern Gulf of Mexico. Interpretation 5,
777 SD25–SD38.
778 Dooley, T.P., Hudec, M.R., Carruthers, D., Jackson, M.P.A., Luo, G., 2017. The effects of base-
779 salt relief on salt flow and suprasalt deformation patterns—Part 1: Flow across simple steps
780 in the base of salt. Interpretation 5, SD1–SD23.
781 Dooley, T.P., Ken, M., Mark, H., Dirk, S., 2004. Basement Controls on Salt Tectonics: Results
782 from Analog Modeling.
783 El Khrepy, S., Koulakov, I., Gerya, T., Al-Arifi, N., Alajmi, M.S., Qadrouh, A.N., 2021. Transition
784 from continental rifting to oceanic spreading in the northern Red Sea area. Scientific Reports

785 11, 1–7.
786 Feldens, P., Mitchell, N.C., 2015. Salt flows in the central Red Sea. The Red Sea. Springer, 205–
787 218.
788 Fiduk, J.C., Rowan, M.G., 2012. Analysis of folding and deformation within layered evaporites in
789 Blocks BM-S-8 &-9, Santos Basin, Brazil. Geological Society, London, Special Publications
790 363, 471–487.
791 Ford, M., Vergés, J., 2021. Evolution of a salt-rich transtensional rifted margin, eastern North
792 Pyrenees, France. Journal of the Geological Society 178, jgs2019-157.
793 Gaulier, J.M., Le Pichon, X., Lyberis, N., Avedik, F., Geli, L., Moretti, I., Deschamps, A., Hafez,
794 S., 1988. Seismic study of the crust of the northern Red Sea and Gulf of Suez. Tectonophysics
795 153, 55–88.
796 Girdler, R.W., Underwood, M., 1985. The evolution of early oceanic lithosphere in the southern
797 Red Sea. Tectonophysics 116, 95–108.
798 Girdler, R.W., Whitmarsh, R., 1974. Miocene Evaporites in Red Sea cores, their relavance to the
799 problem of the width and age of oceanic crust beneath the Red Sea.
800 Gordon, G., Hansen, B., Scott, J., Hirst, C., Graham, R., Grow, T., Spedding, A., Fairhead, S.,
801 Fullarton, L., Griffin, D., 2010. The hydrocarbon prospectivity of the Egyptian North Red
802 Sea basin. Geological Society, London, Petroleum Geology Conference Series. Geological
803 Society of London, 783–789.
804 Griffin, D.L., 2002. Aridity and humidity: two aspects of the late Miocene climate of North Africa
805 and the Mediterranean. Palaeogeography, Palaeoclimatology, Palaeoecology 182, 65–91.
806 Griffin, D.L., 1999. The late Miocene climate of northeastern Africa: unravelling the signals in the
807 sedimentary succession. Journal of the Geological Society 156, 817–826.

808 Hansen, T.H., Clausen, O.R., Andresen, K.J., 2021. Thick-and thin-skinned basin inversion in the
809 Danish Central Graben, North Sea–the role of deep evaporites and basement kinematics.
810 Solid Earth 12, 1719–1747.
811 Haq, B.U., Schutter, S.R., 2008. A chronology of Paleozoic sea-level changes. Science 322, 64–
812 68.
813 Heaton, R.C., Jackson, M.P.A., Bamahmoud, M., Nani, A.S.O., 1995. Superposed Neogene
814 extension, contraction, and salt canopy emplacement in the Yemeni Red Sea.
815 Hempton, M.R., 1987. Constraints on Arabian plate motion and extensional history of the Red
816 Sea. Tectonics 6, 687–705.
817 Hovland, M., Rueslåtten, H., Johnsen, H.K., 2015. Red Sea salt formations—a result of
818 hydrothermal processes. The Red Sea. Springer, 187–203.
819 Hughes, G.W. ap G., Johnson, R.S., 2005. Lithostratigraphy of the Red Sea region. GeoArabia 10,
820 49–126.
821 Hughes, G.W., Beydoun, Z.R., 1992. The Red Sea—Gulf of Aden: biostratigraphy,
822 lithostratigraphy and palaeoenvironments. Journal of Petroleum Geology 15, 135–156.
823 Izzeldin, A.Y., 1987. Seismic, gravity and magnetic surveys in the central part of the Red Sea:
824 their interpretation and implications for the structure and evolution of the Red Sea.
825 Tectonophysics 143, 269–306.
826 Jackson, C.A.-L., Jackson, M.P.A., Hudec, M.R., Rodriguez, C.R., 2015. Enigmatic structures
827 within salt walls of the Santos Basin—Part 1: Geometry and kinematics from 3D seismic
828 reflection and well data. Journal of Structural Geology 75, 135–162.
829 Jackson, M.P.A., Vendeville, B.C., 1994. Regional extension as a geologic trigger for diapirism.
830 Geological Society of America Bulletin 106, 57–73.

831 Jarrige, J., Ott d'Estevou, P., Burollet, P.F., Montenat, C., Prat, P., Richert, J., Thiriet, J., 1990.
832 The multistage tectonic evolution of the Gulf of Suez and northern Red Sea continental rift
833 from field observations. Tectonics 9, 441–465.
834 Khalil, S.M., McClay, K.R., 2009. Structural control on syn-rift sedimentation, northwestern Red
835 Sea margin, Egypt. Marine and Petroleum Geology 26, 1018–1034.
836 Khalil, S.M., McClay, K.R., 2002. Extensional fault-related folding, northwestern Red Sea, Egypt.
837 Journal of Structural Geology 24, 743–762.
838 Khalil, S.M., McClay, K.R., 2001. Tectonic evolution of the NW Red Sea-Gulf of Suez rift system.
839 Geological Society, London, Special Publications 187, 453–473.
840 Koyi, H., 1991. Gravity overturns, extension, and basement fault activation. Journal of Petroleum
841 Geology 14, 117–142.
842 Koyi, H., Jenyon, M.K., Petersen, K., 1993a. The effect of basement faulting on diapirism. Journal
843 of Petroleum Geology 16, 285–312.
844 Koyi, H., Petersen, K., 1993. Influence of basement faults on the development of salt structures in
845 the Danish Basin. Marine and Petroleum Geology 10, 82–94.
846 Koyi, H., Talbot, C.J., Tørudbakken, B.O., 1993b. Salt diapirs of the southwest Nordkapp Basin:
847 analogue modelling. Tectonophysics 228, 167–187.
848 Koyi, H.A., 2001. Modeling the influence of sinking anhydrite blocks on salt diapirs targeted for
849 hazardous waste disposal. Geology 29, 387–390.
850 Le Magoarou, C., Hirsch, K., Fleury, C., Martin, R., Ramirez-Bernal, J., Ball, P., 2021. Integration
851 of gravity, magnetic, and seismic data for subsalt modeling in the Northern Red Sea.
852 Interpretation 9, T507–T521.
853 Li, Z., Schieber, J., 2022. Correlative conformity or subtle unconformity? The distal expression of

854 a sequence boundary in the Upper Cretaceous Mancos Shale, Henry Mountains Region, Utah,
855 USA. Journal of Sedimentary Research 92, 635–657.
856 Ligi, M., Bonatti, E., Bortoluzzi, G., Cipriani, A., Cocchi, L., Caratori Tontini, F., Carminati, E.,
857 Ottolini, L., Schettino, A., 2012. Birth of an ocean in the Red Sea: initial pangs.
858 Geochemistry, Geophysics, Geosystems 13.
859 Ligi, M., Bonatti, E., Bosworth, W., Cai, Y., Cipriani, A., Palmiotto, C., Ronca, S., Seyler, M.,
860 2018. Birth of an ocean in the Red Sea: Oceanic-type basaltic melt intrusions precede
861 continental rupture. Gondwana Research 54, 150–160.
862 Lyberis, N., 1988. Tectonic evolution of the Gulf of Suez and the Gulf of Aqaba. Tectonophysics
863 153, 209–220.
864 M. Pichel, L., Finch, E., Gawthorpe, R.L., 2019. The impact of pre- salt rift topography on salt
865 tectonics: A discrete- element modeling approach. Tectonics 38, 1466–1488.
866 Mahmoud, S., Reilinger, R., McClusky, S., Vernant, P., Tealeb, A., 2005. GPS evidence for
867 northward motion of the Sinai Block: implications for E. Mediterranean tectonics. Earth and
868 Planetary Science Letters 238, 217–224.
869 Mahsoub, M., Abulnasr, R., Boukhary, M., Faris, M., Abd El Aal, M., 2012. Bio-and sequence
870 stratigraphy of upper cretaceous–palaeogene rocks, east Bahariya concession, Western
871 Desert, Egypt. Geologia Croatica 65, 109–138.
872 Makris, J., Rihm, R., 1991. Shear-controlled evolution of the Red Sea: pull apart model.
873 Tectonophysics 198, 441–466.
874 Mart, Y., Hall, J.K., 1984. Structural trends in the northern Red Sea. Journal of Geophysical
875 Research: Solid Earth 89, 11352–11364.
876 Mart, Y., Ross, D.A., 1987. Post-Miocene rifting and diapirism in the northern Red Sea. Marine

877 Geology 74, 173–190.
878 Masini, E., Stockli, D., Gómez-Romeu, J., Ball, P., Kusznir, N.J., Calassou, S., 2020. Exploration
879 challenges and perspectives of hyper-extended rift systems: A Northern Red Sea viewpoint.
880 AAPG Middle East Region Geoscience Technology Workshop, Rift Basin Evolution and
881 Exploration.
882 McClay, K.R., 1996. Recent advances in analogue modelling: uses in section interpretation and
883 validation. Geological Society, London, Special Publications 99, 201–225.
884 McClay, K.R., Scott, A.D., 1991. Experimental models of hangingwall deformation in ramp-flat
885 listric extensional fault systems. Tectonophysics 188, 85–96.
886 McKenzie, D.P., Davies, D., Molnar, P., 1970. Plate tectonics of the Red Sea and east Africa.
887 Nature 226, 243–248.
888 Miller, P.M., Barakat, H., 1988. Geology of the safaga concession, northern Red Sea, Egypt.
889 Tectonophysics 153, 123–136.
890 Mitchell, N.C., Hernandez, K., Preine, J., Ligi, M., Augustin, N., Izzeldin, A., Hübscher, C., 2022.
891 Early stage diapirism in the Red Sea deep-water evaporites: Origins and length-scales.
892 Tectonophysics 831, 229331.
893 Mitchell, N.C., Ligi, M., Feldens, P., Hübscher, C., 2017. Deformation of a young salt giant:
894 regional topography of the R ed S ea M iocene evaporites. Basin Research 29, 352–369.
895 Mitchell, N.C., Ligi, M., Ferrante, V., Bonatti, E., Rutter, E., 2010. Submarine salt flows in the
896 central Red Sea. Bulletin 122, 701–713.
897 Mitchell, N.C., Ligi, M., Rasul, N.M.A., 2019. Variations in Plio-Pleistocene Deposition in the
898 Red Sea. Geological Setting, Palaeoenvironment and Archaeology of the Red Sea. Springer,
899 323–339.

900 Mitchell, N.C., Park, Y., 2014. Nature of crust in the central Red Sea. Tectonophysics 628, 123–
901 139.
902 Mitchell, N.C., Shi, W., Izzeldin, A.Y., Stewart, I.C.F., 2021. Reconstructing the level of the
903 central Red Sea evaporites at the end of the Miocene. Basin Research 33, 1266–1292.
904 Mohriak, W., 2019. Rifting and salt deposition on continental margins: Differences and similarities
905 between the Red Sea and the South Atlantic sedimentary basins. Geological Setting,
906 Palaeoenvironment and Archaeology of the Red Sea 159–201.
907 Mohriak, W., 2014. Birth and development of continental margin basins: Analogies from the South
908 Atlantic, North Atlantic, and the Red Sea. AAPG Search Discov. Artic 41502.
909 Montenat, C., D'Estevou, P.O., Purser, B., Burollet, P.-F., Jarrige, J.-J., Orszag-Sperber, F.,
910 Philobbos, E., Plaziat, J.-C., Prat, P., Richert, J.-P., 1988. Tectonic and sedimentary evolution
911 of the Gulf of Suez and the northwestern Red Sea. Tectonophysics 153, 161–177.
912 Moustafa, A.R., Khalil, S.M., 2020. Structural Setting and Tectonic Evolution of the Gulf of Suez,
913 NW Red Sea and Gulf of Aqaba Rift Systems. The Geology of Egypt. Springer, 295–342.
914 Muzaffar, A., Keller, J., Borsato, R., 2018. Structural characterization of the Middle Miocene
915 Mansiyah salt in the Red Sea. EGU General Assembly Conference Abstracts. 2202.
916 Nilsen, K.T., Vendeville, B.C., Johansen, J.-T., 1995. Influence of regional tectonics on
917 halokinesis in the Nordkapp Basin, Barents Sea.
918 Orszag-Sperber, F., Harwood, G., Kendall, A., Purser, B.H., 1998. A review of the evaporites of
919 the Red Sea-Gulf of Suez rift. Sedimentation and Tectonics in Rift Basins Red Sea:-Gulf of
920 Aden. Springer, 409–426.
921 Patton, T.L., Moustafa, A.R., Nelson, R.A., Abdine, S.A., 1994. Tectonic evolution and structural
922 setting of the Suez Rift: Chapter 1: Part I. Type Basin: Gulf of Suez.

923 Pichel, L.M., Peel, F., Jackson, C.A.L., Huuse, M., 2018. Geometry and kinematics of salt-
924 detached ramp syncline basins. Journal of Structural Geology 115, 208–230.
925 Richter, H., Makris, J., Rihm, R., 1991. Geophysical observations offshore Saudi Arabia: seismic
926 and magnetic measurements. Tectonophysics 198, 297–310.
927 Rihm, R., Makris, J., Möller, L., 1991. Seismic surveys in the Northern Red Sea: asymmetric
928 crustal structure. Tectonophysics 198, 279–295.
929 Rojo, L.A., Cardozo, N., Escalona, A., Koyi, H., 2019. Structural style and evolution of the
930 Nordkapp Basin, Norwegian Barents Sea. Aapg Bulletin 103, 2177–2217.
931 Rojo, L.A., Escalona, A., 2018. Controls on minibasin infill in the Nordkapp Basin: Evidence of
932 complex Triassic synsedimentary deposition influenced by salt tectonics. Aapg Bulletin 102,
933 1239–1272.
934 Rojo, L.A., Koyi, H., Cardozo, N., Escalona, A., 2020. Salt tectonics in salt-bearing rift basins:
935 Progradational loading vs extension. Journal of Structural Geology 141, 104193.
936 Ross, D.A., Schlee, J., 1973. Shallow structure and geologic development of the southern Red Sea.
937 Geological Society of America Bulletin 84, 3827–3848.
938 Rowan, M.G., 2014. Passive- margin salt basins: Hyperextension, evaporite deposition, and salt
939 tectonics. Basin Research 26, 154–182.
940 Saleh, S., Jahr, T., Jentzsch, G., Saleh, A., Abou Ashour, N.M., 2006. Crustal evaluation of the
941 northern Red Sea rift and Gulf of Suez, Egypt from geophysical data: 3-dimensional
942 modeling. Journal of African Earth Sciences 45, 257–278.
943 Schettino, A., Macchiavelli, C., Pierantoni, P.P., Zanoni, D., Rasul, N., 2016. Recent kinematics
944 of the tectonic plates surrounding the Red Sea and Gulf of Aden. Geophysical Journal
945 International 207, 457–480.

946 Schettino, A., Macchiavelli, C., Rasul, N.M.A., 2019. Plate motions around the Red Sea since the
947 Early Oligocene. Geological Setting, Palaeoenvironment and Archaeology of the Red Sea
948 203–220.
949 Smith, J.E., Santamarina, J.C., 2022. Red sea evaporites: Formation, creep and dissolution. Earth-
950 Science Reviews 104115.
951 Sultan, M., Becker, R., Arvidson, R.E., Shore, P., Stern, R.J., El Alfy, Z., Guinness, E.A., 1992.
952 Nature of the Red Sea crust: a controversy revisited. Geology 20, 593–596.
953 Tewfik, N., Ayyad, M., 1982. Petroleum exploration in the Red Sea shelf of Egypt. Proc. 6th
954 Exploration Seminar, Egyptian General Petroleum Corporation and Egypt Petroleum
955 Exploration Society, Cairo. 159–180.
956 Tubbs, R.E., Fouda, H.G.A., Afifi, A.M., Raterman, N.S., Hughes, G.W., Fadolalkarem, Y.K.,
957 2014. Midyan Peninsula, northern Red Sea, Saudi Arabia: seismic imaging and regional
958 interpretation. GeoArabia 19, 165–184.
959 van Hinsbergen, D.J.J., De Groot, L. V, van Schaik, S.J., Spakman, W., Bijl, P.K., Sluijs, A.,
960 Langereis, C.G., Brinkhuis, H., 2015. A paleolatitude calculator for paleoclimate studies.
961 PloS One 10, e0126946.
962 Vendeville, B.C., Jackson, M.P.A., 1992a. The rise of diapirs during thin-skinned extension.
963 Marine and Petroleum Geology 9, 331–354.
964 Vendeville, B.C., Jackson, M.P.A., 1992b. The fall of diapirs during thin-skinned extension.
965 Marine and Petroleum Geology 9, 354–371.
966 Warren, J.K., 2010. Evaporites through time: Tectonic, climatic and eustatic controls in marine
967 and nonmarine deposits. Earth-Science Reviews 98, 217–268.
968 Withjack, M.O., Callaway, S., 2000. Active normal faulting beneath a salt layer: an experimental

study of deformation patterns in the cover sequence. AAPG Bulletin 84, 627–651.

Withjack, M.O., Olson, J., Peterson, E., 1990. Experimental models of extensional forced folds. Aapg Bulletin 74, 1038–1054.

992

993 **Figures caption**

994 Figure 1. (a) Plate tectonic setting of the Red Sea, Gulf of Aden, Gulf of Suez, and Gulf of Aqaba.
995 Modified from Hempton (1987), Khalil and McClay (2002), and Bosworth et al. (2005).
996 Blue arrows denote plate movement directions after Mahmoud et al. (2005) and ArRajehi
997 et al. (2010). ZI is Zabargad Island, ZFZ is Zabargad Fracture Zone, and AF is Alula-Fartak
998 Fracture Zone. (b) Geological map of the northern Red Sea showing the main structural
999 elements (modified from Bosworth et al., 2017). The red box represents the study area.

1000 Figure 2. Stratigraphic column of the offshore northern Red Sea (modified from Bosworth et al.,
1001 2020). Blue lines denote the interpreted seismic horizons.

1002 Figure 3. Bathymetric map of the central part of the Egyptian rifted margin, and location of wells
1003 and seismic sections used in this study. The shaded area indicates the available 3D seismic
1004 survey. The dashed black lines represent the interpreted crosslines. Yellow lines show
1005 location of 2D seismic profiles, and blue points indicate location of wells used to tie with
1006 them.

1007 Figure 4. Summary scheme showing rift episodes and the deposition time of the evaporites, as well
1008 as the magmatism stages in the northern Red Sea, modified after Ali et al. (2023). Sea-level
1009 curve from Haq and Schutter (2008) and Paleo-latitudes from van Hinsbergen et al. (2015).

1010 Figure 5. (a) Uninterpreted and (b) Interpreted crossline 3200, depicting pre-salt sediments and
1011 salt diapirs. D1 salt diapir roots to a narrow horst. Note two Quaternary volcanoes on the
1012 northeastern side of the profile. White lines indicate normal faults. D, ID, and SB denote

1013 diapir, immature diaper, and subbasin, respectively. Section location is shown in Figure 3.
1014 VE: vertical exaggeration.

1015 Figure 6. (a) Uninterpreted and (b) Interpreted crossline 3900, displaying extensional faults (white
1016 lines), mature (D) and immature (ID) salt structures, and unconformity surface above the
1017 layered evaporites. SB denotes subbasin. Section location is shown in Figure 3. VE:
1018 vertical exaggeration.

1019 Figure 7. (a) Uninterpreted and (b) Interpreted crossline 4450, crossing the central part of the
1020 offshore Quseir in a NE-SW. The section shows a major horst, two salt diapirs, and many
1021 subsalt and suprasalt faults (white lines). D and SB denote diapir and subbasin,
1022 respectively. Section location is shown in Figure 3. VE: vertical exaggeration.

1023 Figure 8. (a) Uninterpreted and (b) Interpreted crossline 5000, displaying extensional faults (white
1024 lines), salt structures, and depocenters migration of the Plio-Quaternary sediments. D and
1025 SB denote diapir and subbasin, respectively. Section location is shown in Figure 3. VE:
1026 vertical exaggeration.

1027 Figure 9. (a) Uninterpreted and (b) Interpreted crossline 5500, depicting normal faults (white
1028 lines), a salt diapir (D), and depocenters migration of the Plio-Quaternary sequence. SB
1029 denotes subbasin. Section location is shown in Figure 3. VE: vertical exaggeration.

1030 Figure 10. (a) Uninterpreted and (b) Interpreted NE-SW seismic profile, passing through the
1031 margin. The section shows shallow and deep detachment faults, D1 and D2 salt diapirs root
1032 to narrow horsts, and two different types of ramp-syncline basins. White lines and SB
1033 denote normal faults and subbasin, respectively. Section location is shown in Figure 3. VE:
1034 vertical exaggeration.

1035 Figure 11. (a) Uninterpreted and (b) Interpreted crossline 6300, showing a salt diapir (D) and
1036 normal faults (white lines). Note that the larger throw of the northeastern basement fault
1037 compared to the southwestern fault results in a large thickness variation in the overburden
1038 on both sides of the D5. SB denotes subbasin. Section location is shown in Figure 3. VE:
1039 vertical exaggeration.

1040 Figure 12. (a) Uninterpreted and (b) Interpreted NE-SW seismic profile, passing through the
1041 southwestern part of the offshore Quseir. The section depicts depocenters' migration
1042 landwards and normal faults (white lines). D and SB denote diapir and subbasin,
1043 respectively. Section location is shown in Figure 3. VE: vertical exaggeration.

1044 Figure 13. (a) Uninterpreted and (b) Interpreted NNW-SSE seismic profile, displaying salt diapirs
1045 (D), extensional faults (white lines), and large thickness variations of each seismic
1046 sequence. Section location is shown in Figure 3. VE: vertical exaggeration.

1047 Figure 14. Stratigraphic correlation of well RSO-B 96-1 (northwestern part to the offshore Quseir),
1048 well Quseir A-1X (southwestern part to the offshore Quseir), and well Quseir B-1X in the
1049 southeastern part of offshore Quseir. Wells location is shown in Figure 3.

1050 Figure 15. Top (a) and 3D (b) views of the top of the salt layer displaying five salt walls trending
1051 NW-SE to NNW-SSE. D and SB denote diapir and subbasin, respectively. The movie is
1052 attached to the supplementary materials.

1053 Figure 16. Time slices at -2.5 (a), -2.0 (b), -1.8 (c), -1.6 (d), -1.4 (e), and -1.2 s (f) showing the
1054 distribution of salt walls in the offshore Quseir. Blue and red polygons denote the boundary
1055 of salt walls and seamount, respectively. D is diaper, and SB is subbasin.

1056 Figure 17. TWT map of top (a) Plio-Quaternary sediments and (b) layered evaporites.

1057 Figure 18. TWT map of top salt (a) and base salt (b). D is diapir, and SB is subbasin.

1058 Figure 19. Isopach maps of (a) Plio-Quaternary sequence, (b) layered evaporites, and (c) salt layer.

1059 Figure 20. Schematic reconstruction of the southern part of the offshore Quseir from the Middle
1060 Miocene to the present.

Figure 1

Click here to access/download;Figure;Figure 1.pdf

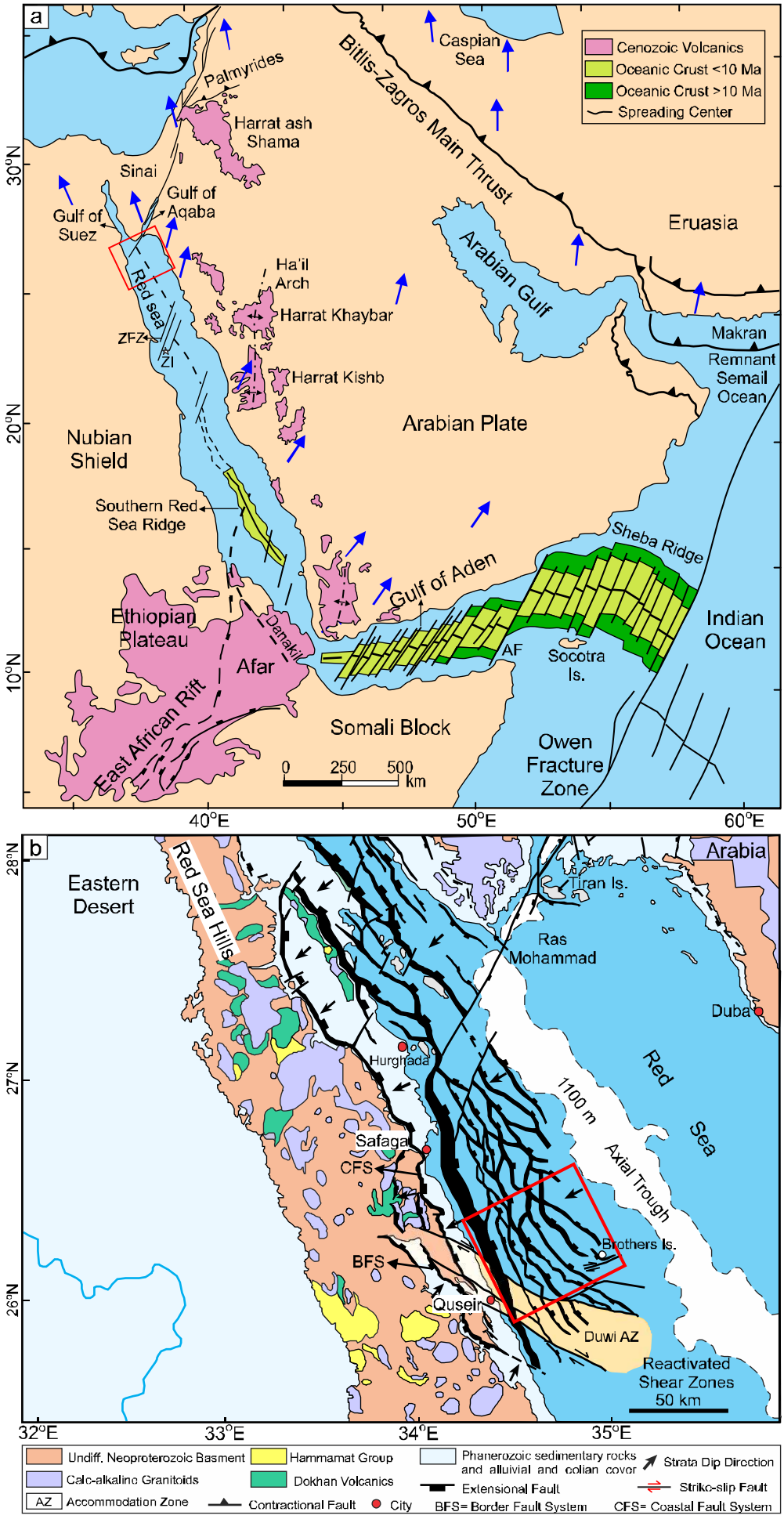

Figure 2

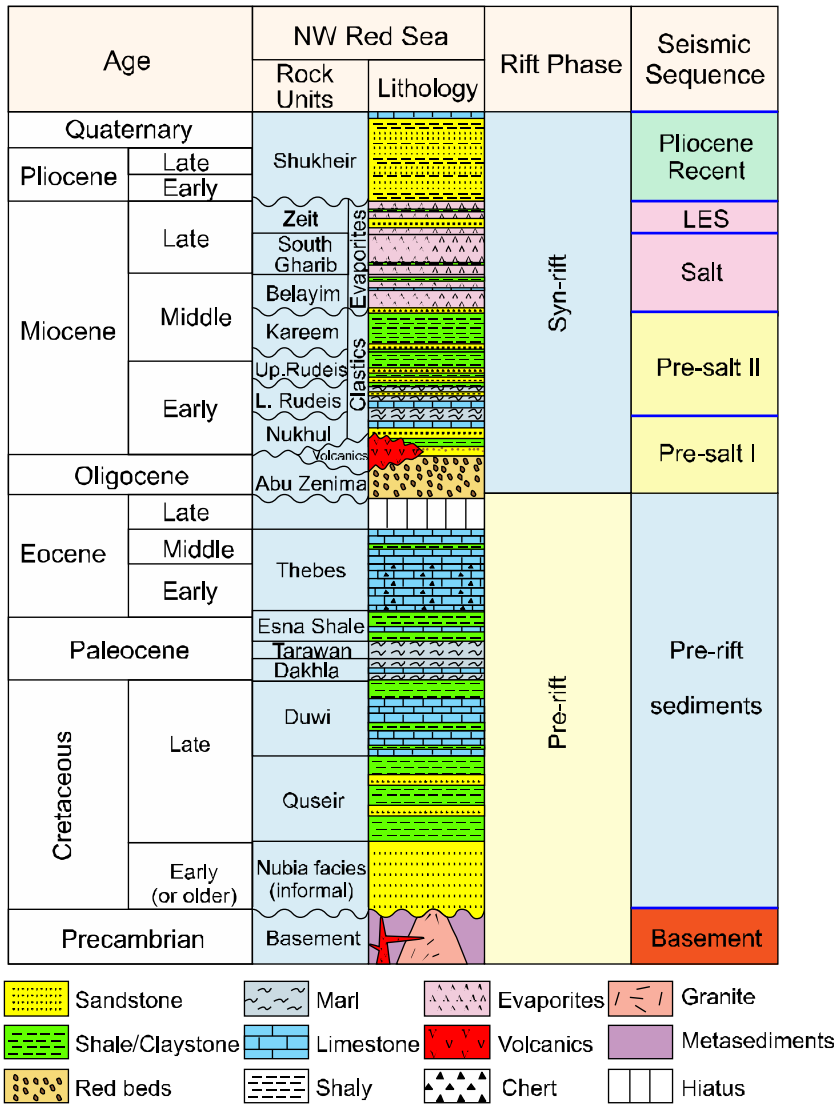

Figure 3

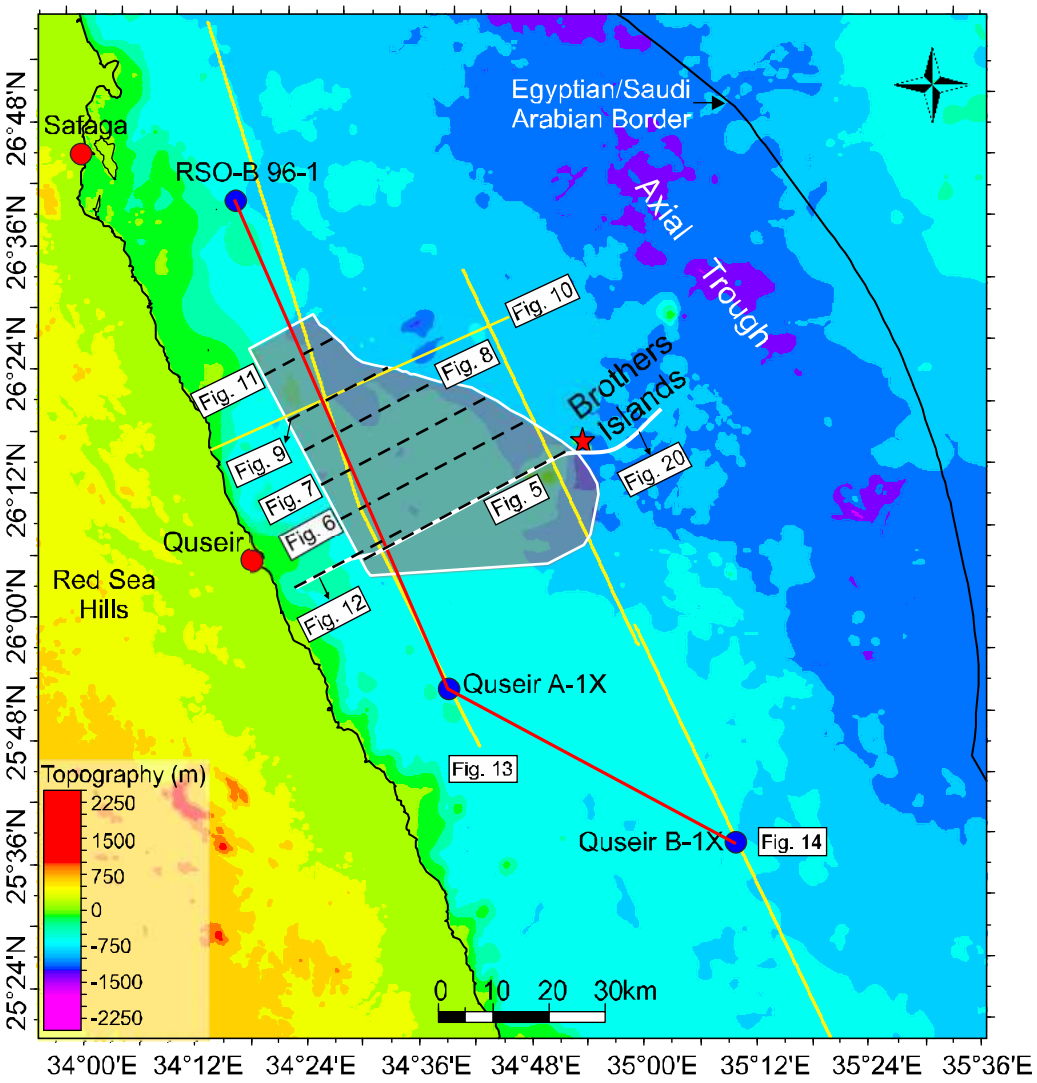

Figure 4

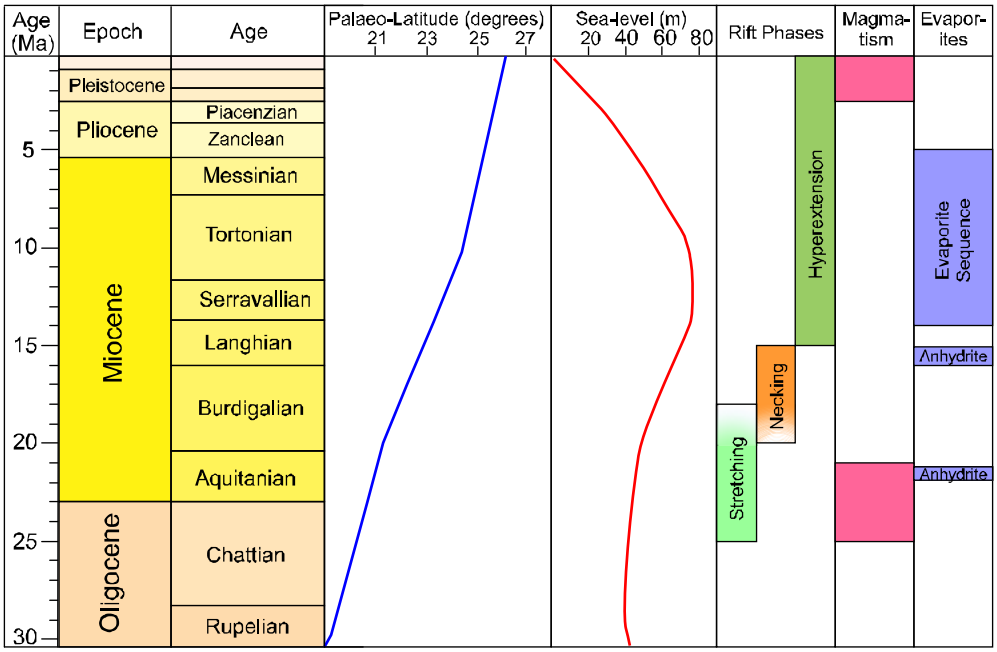

Figure 5

Click here to access/download;Figure;Figure 5.pdf

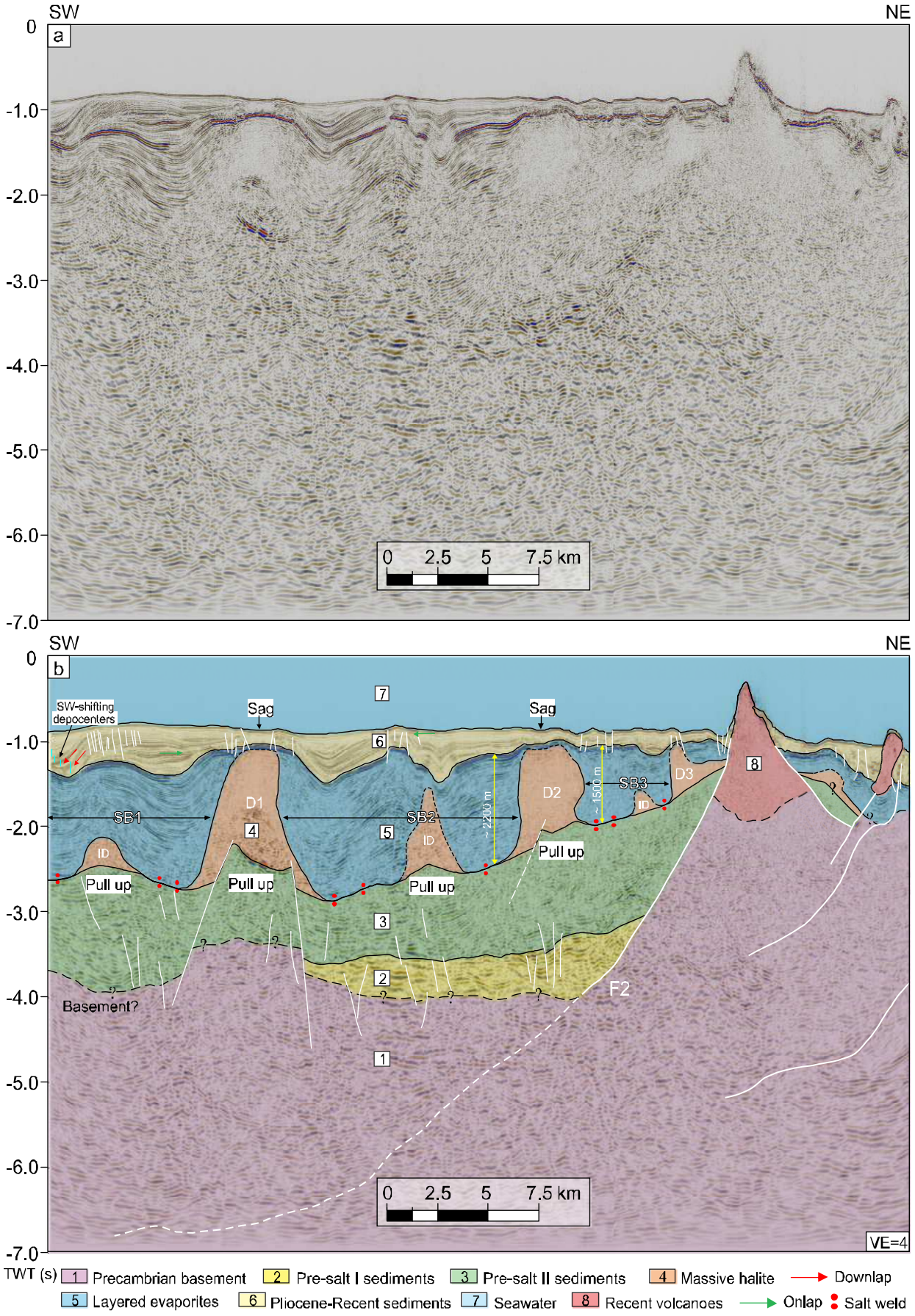

Figure 6

Click here to access/download;Figure;Figure 6.pdf

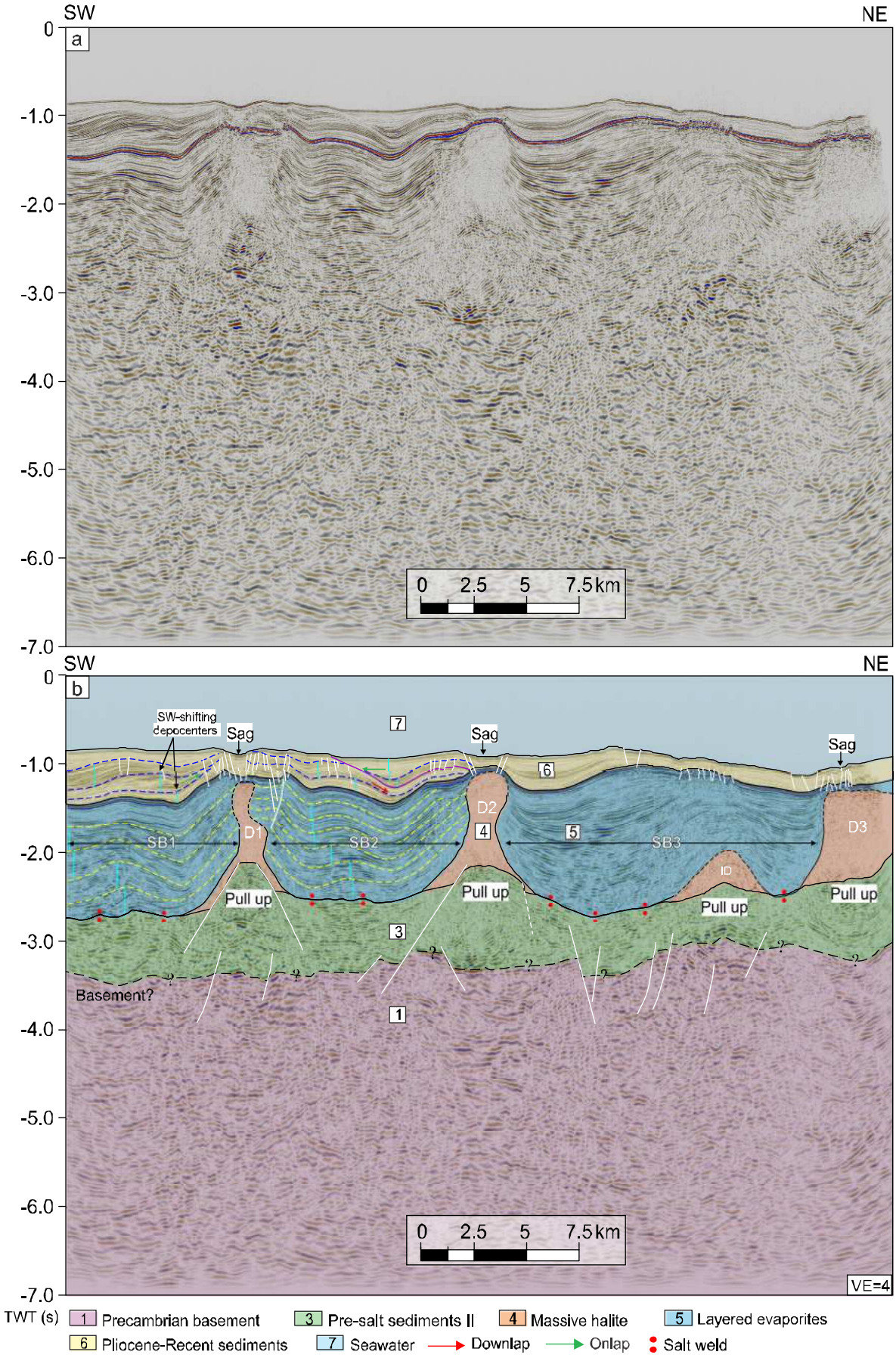

Figure 7

Click here to access/download;Figure;Figure 7.pdf

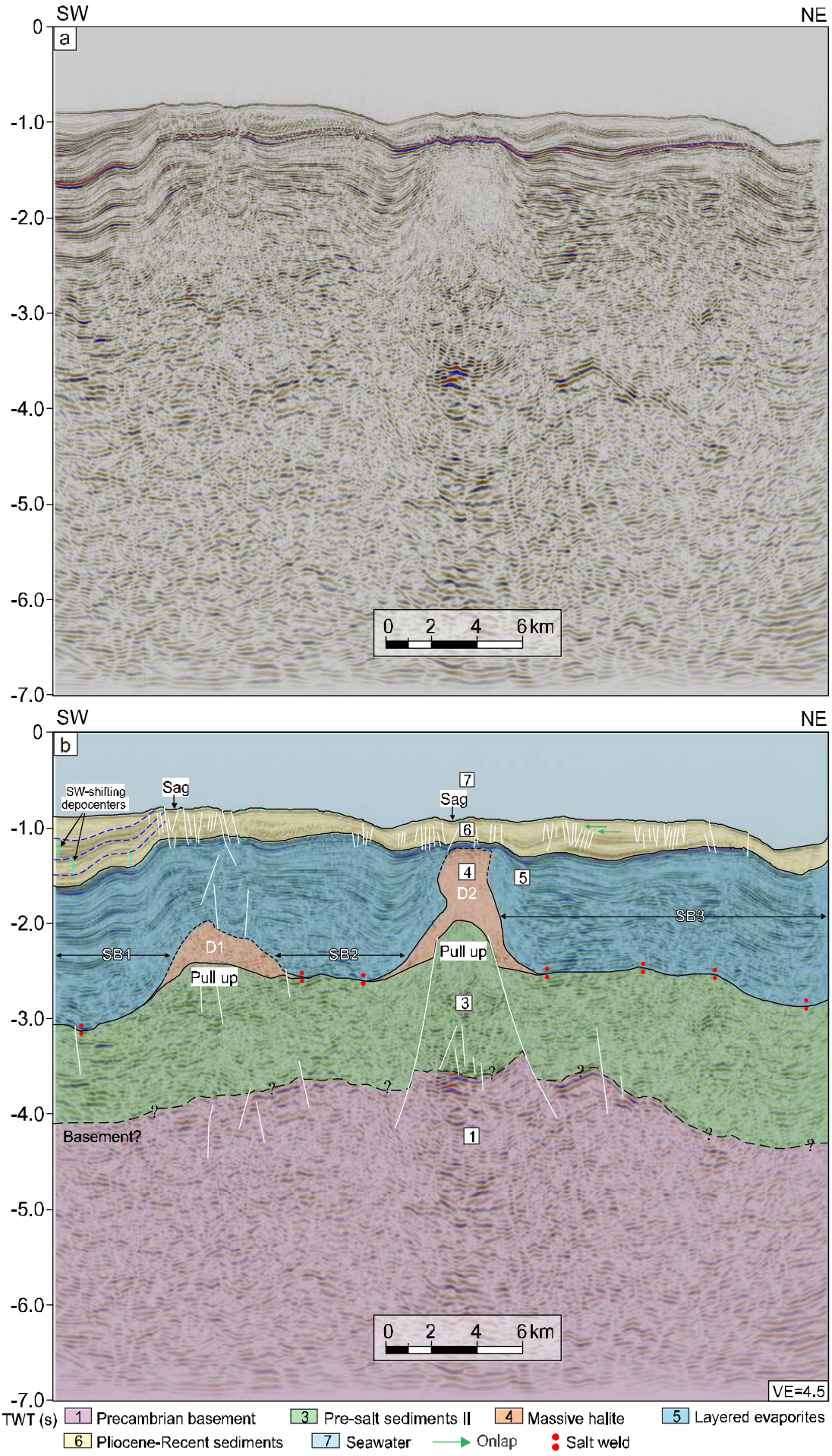

Figure 8

Click here to access/download;Figure;Figure 8.pdf

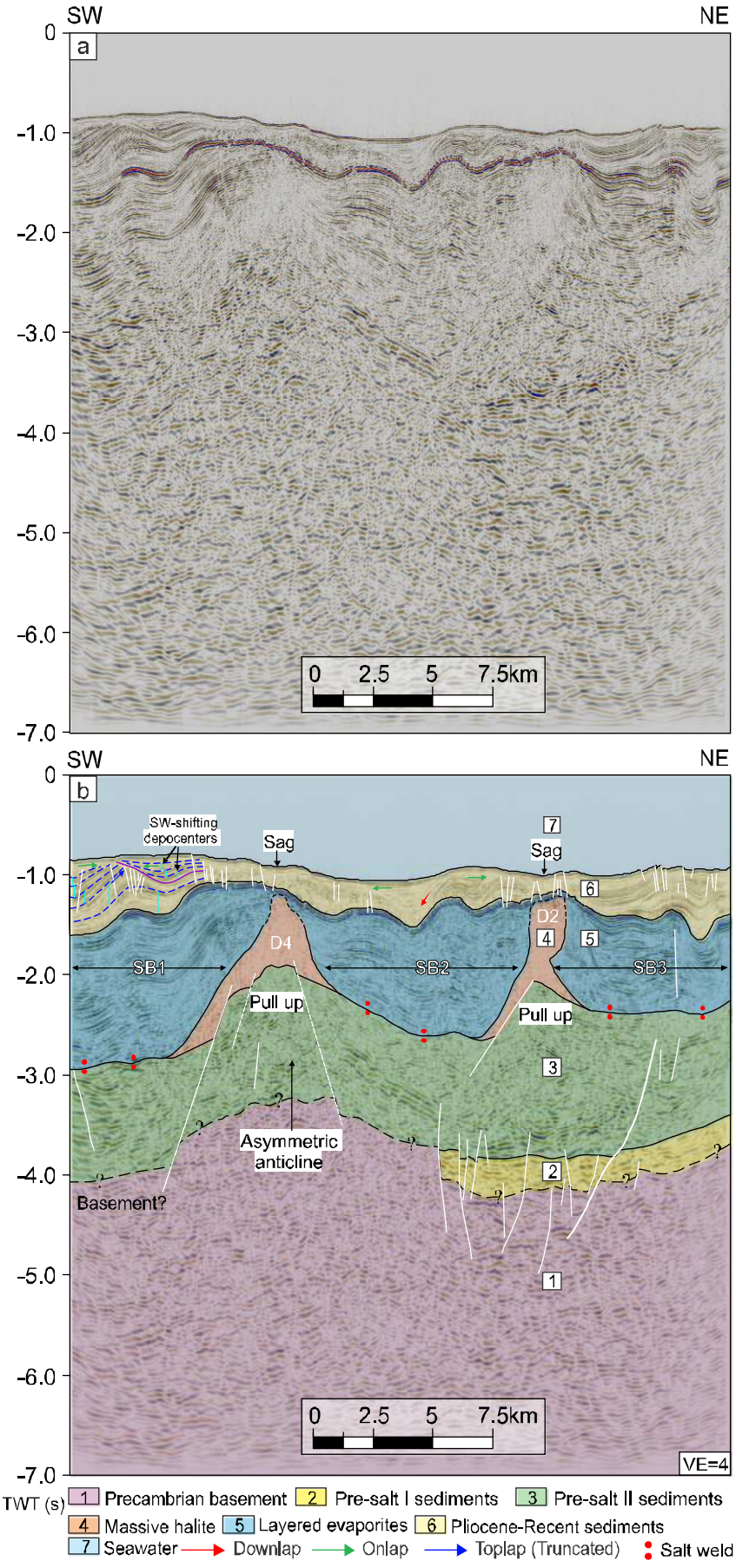

Figure 9

Click here to access/download;Figure;Figure 9.pdf

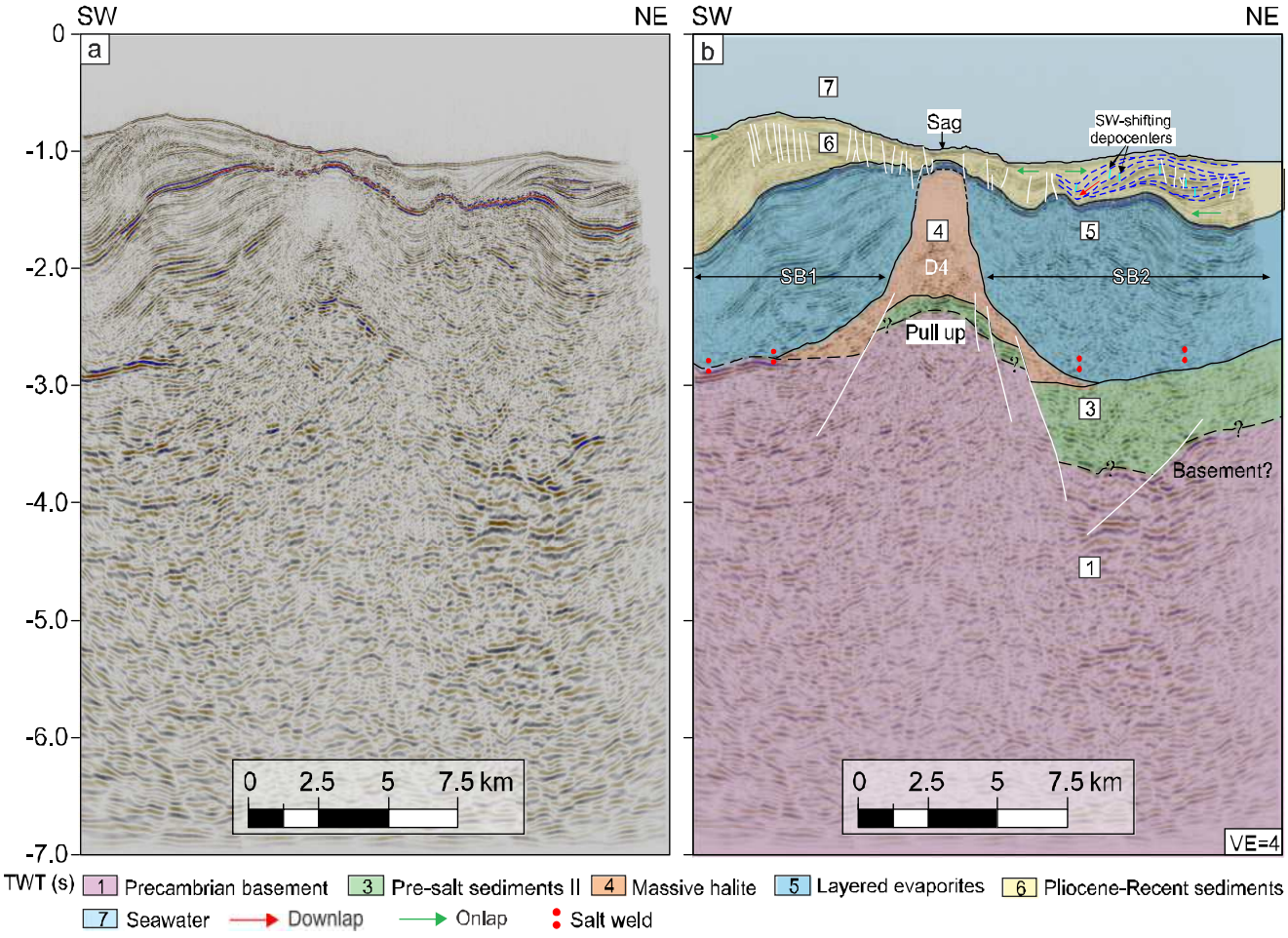

Figure 10

Click here to access/download;Figure;Figure 10.pdf

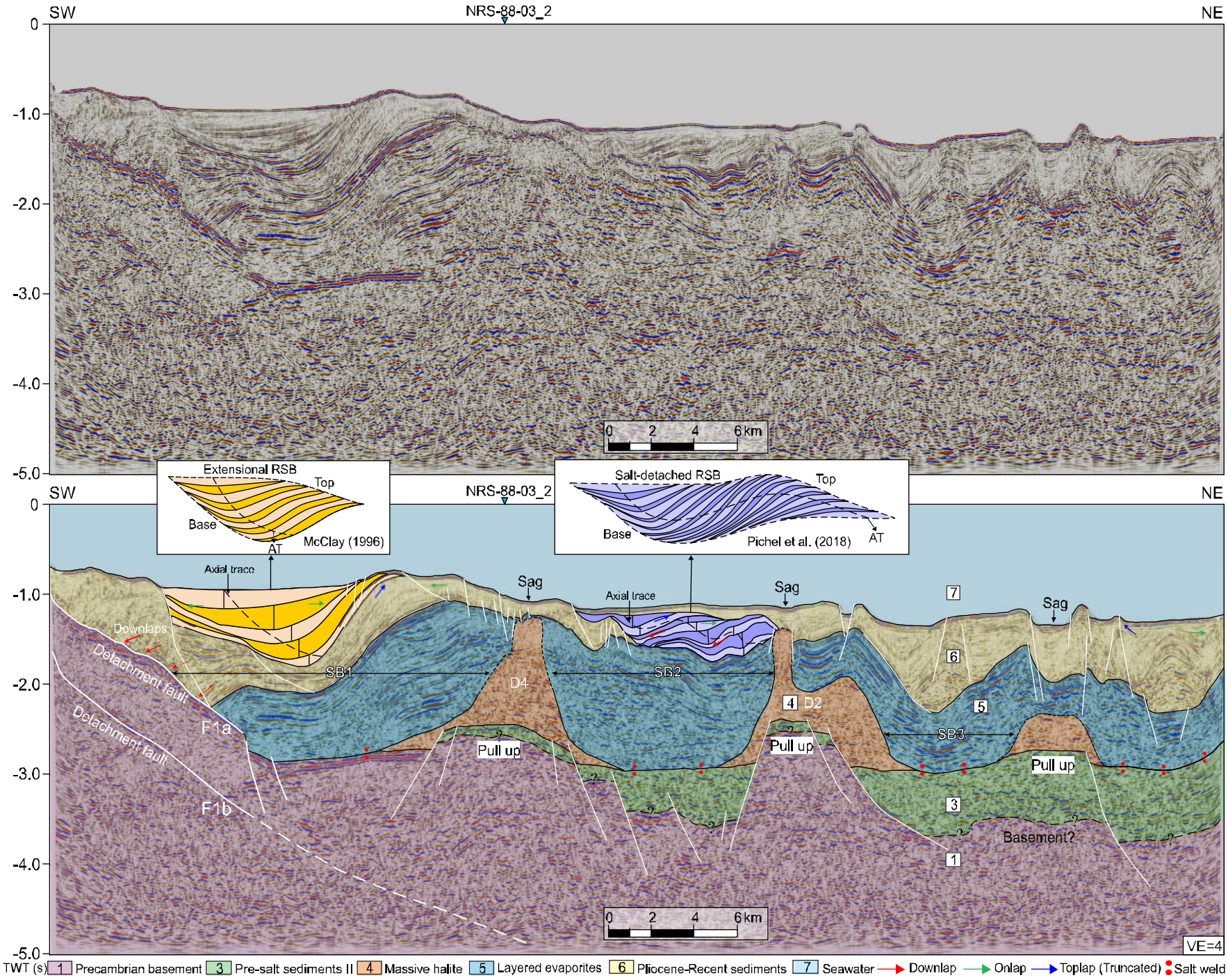

Figure 11

Click here to access/download;Figure;Figure 11.pdf

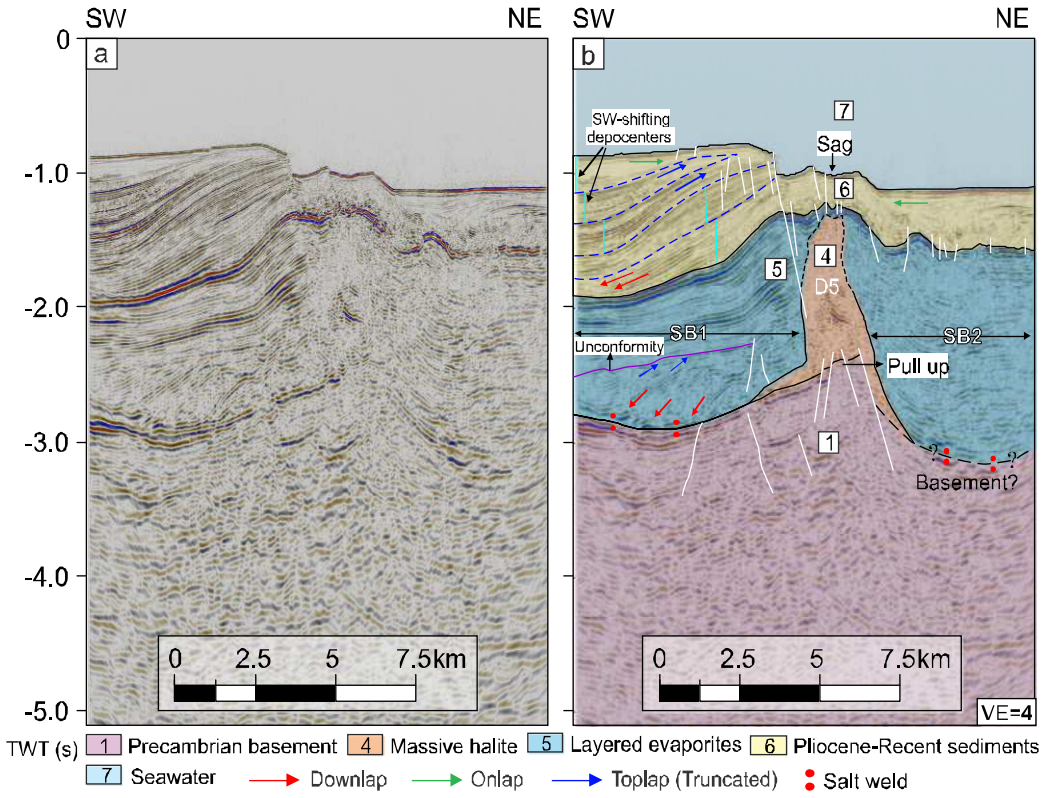

Figure 12

Click here to access/download;Figure;Figure 12.pdf

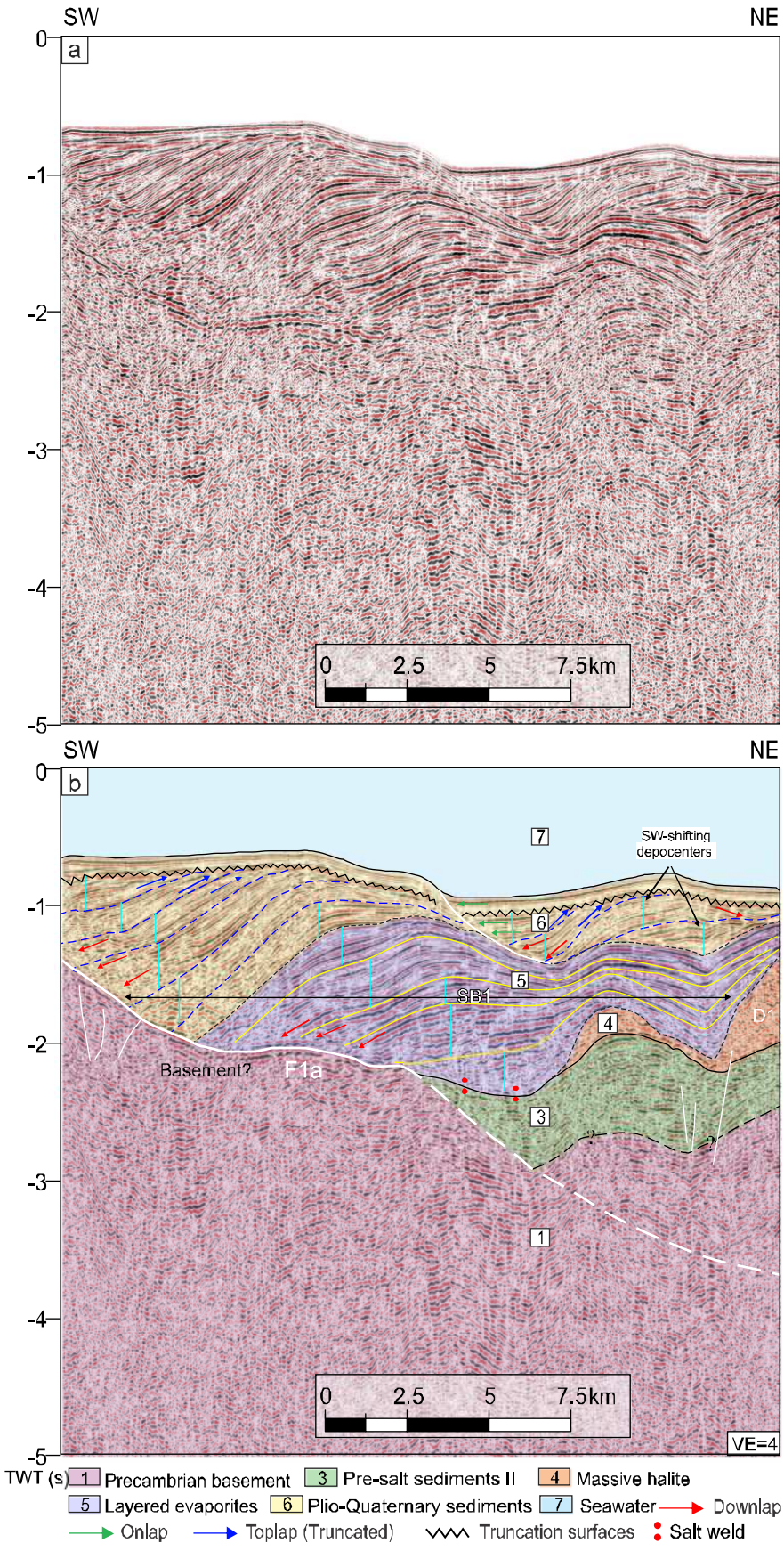

Figure 13

Click here to access/download;Figure;Figure 13.pdf

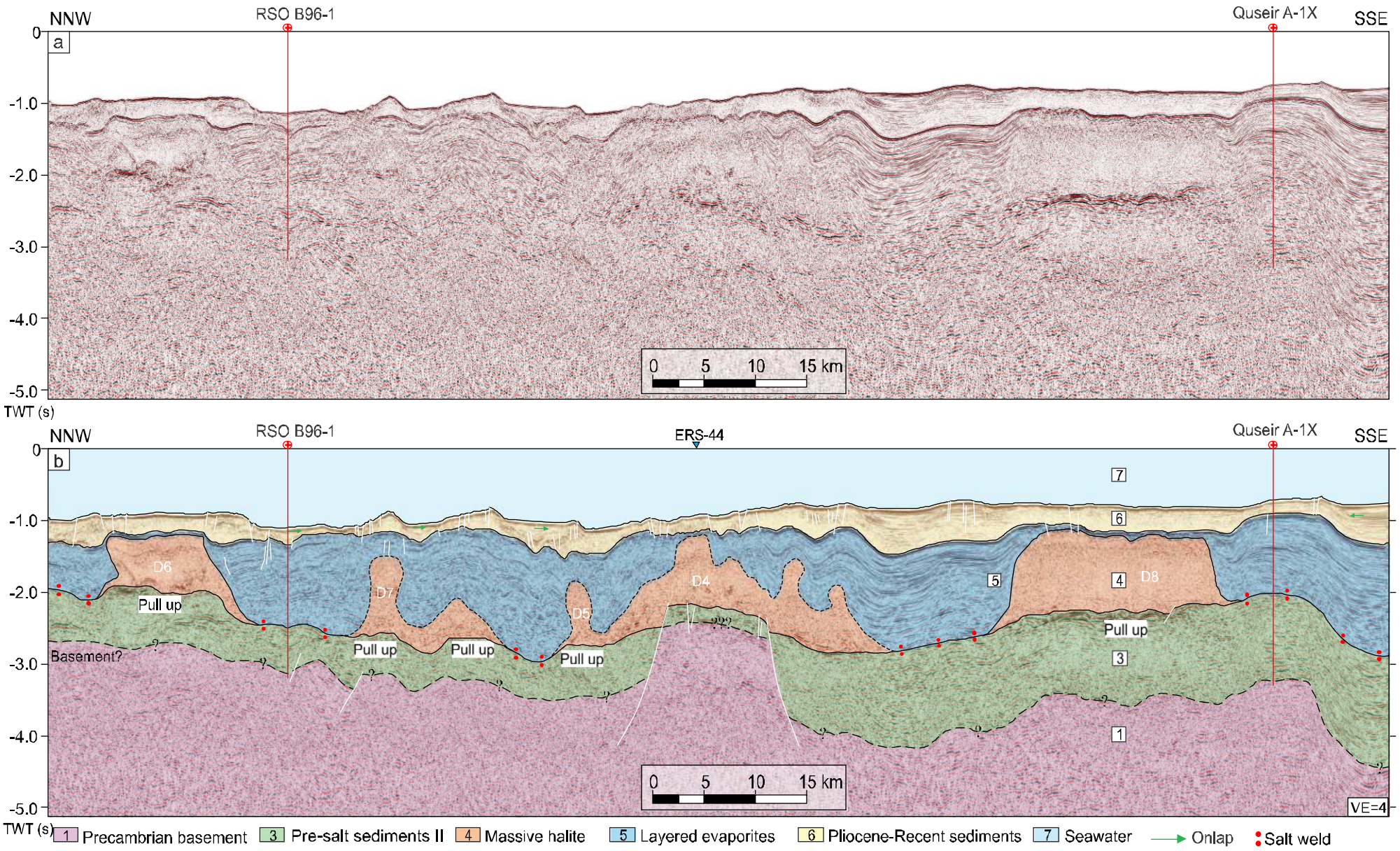

Figure 14

Click here to access/download;Figure;Figure 14.pdf

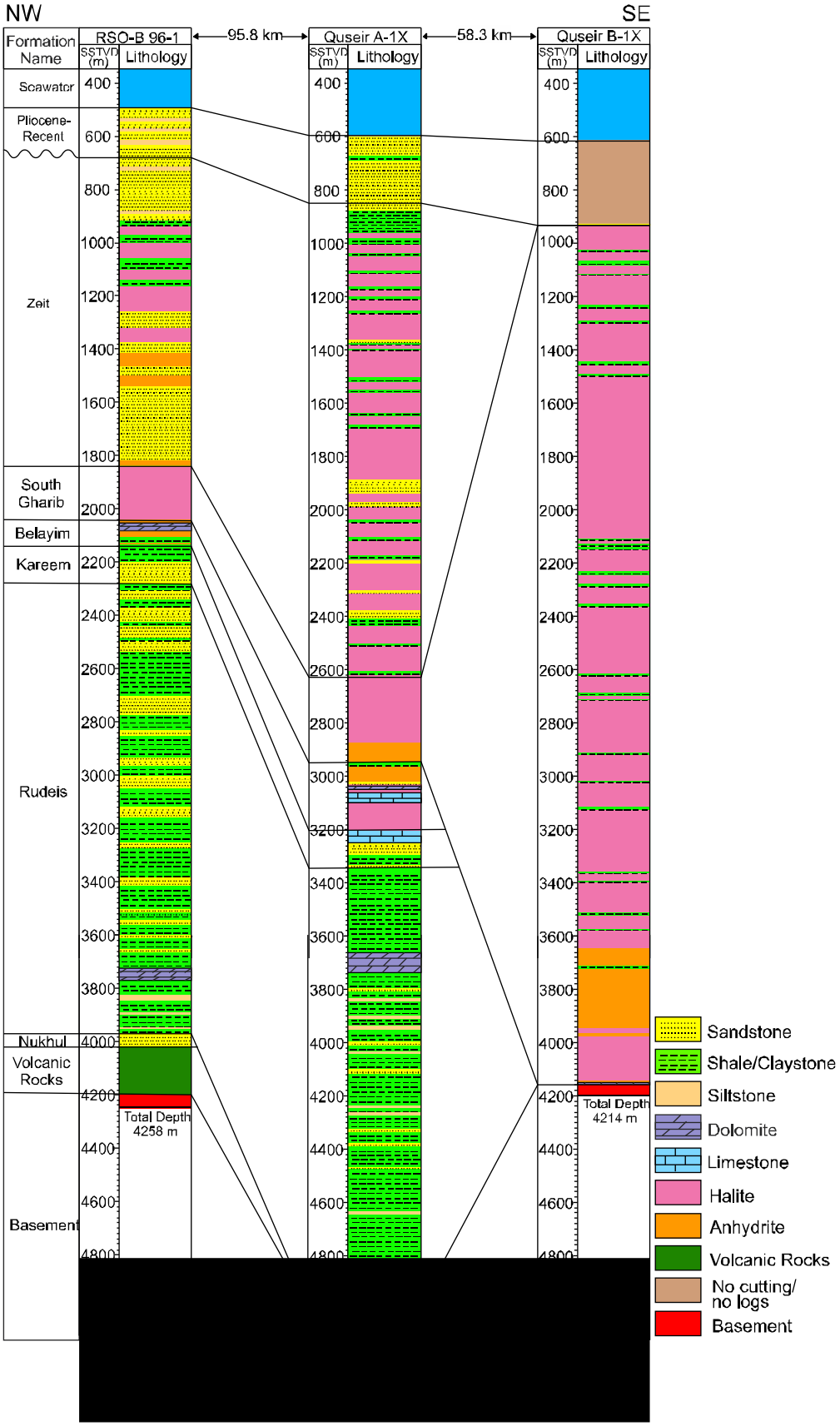

Figure 15

Click here to access/download;Figure;Figure 15.pdf

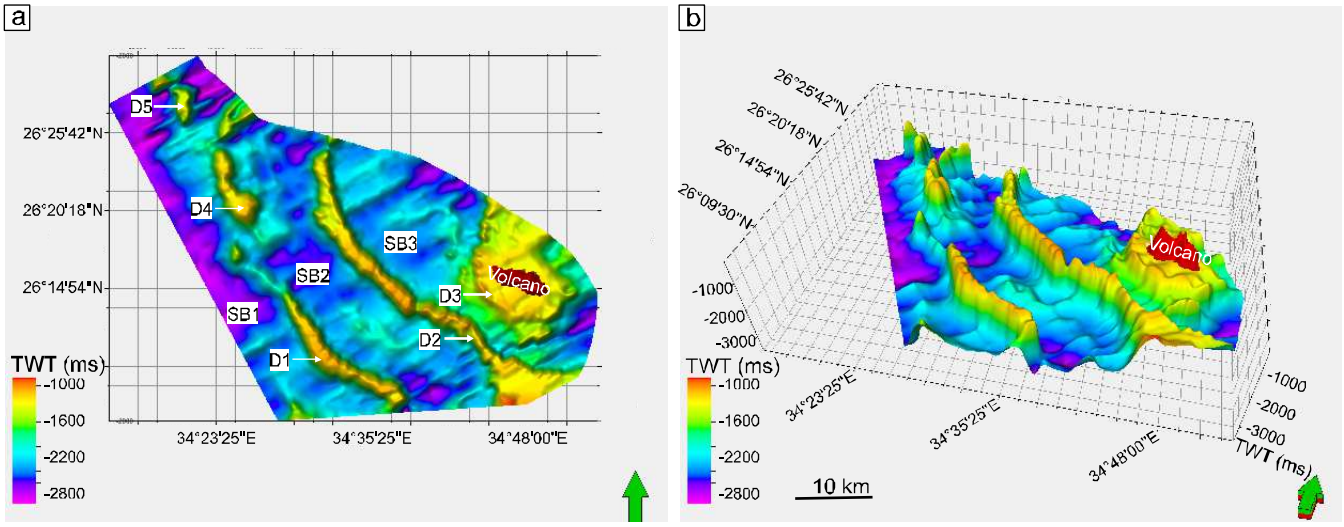

Figure 16

Click here to access/download;Figure;Figure 16.pdf

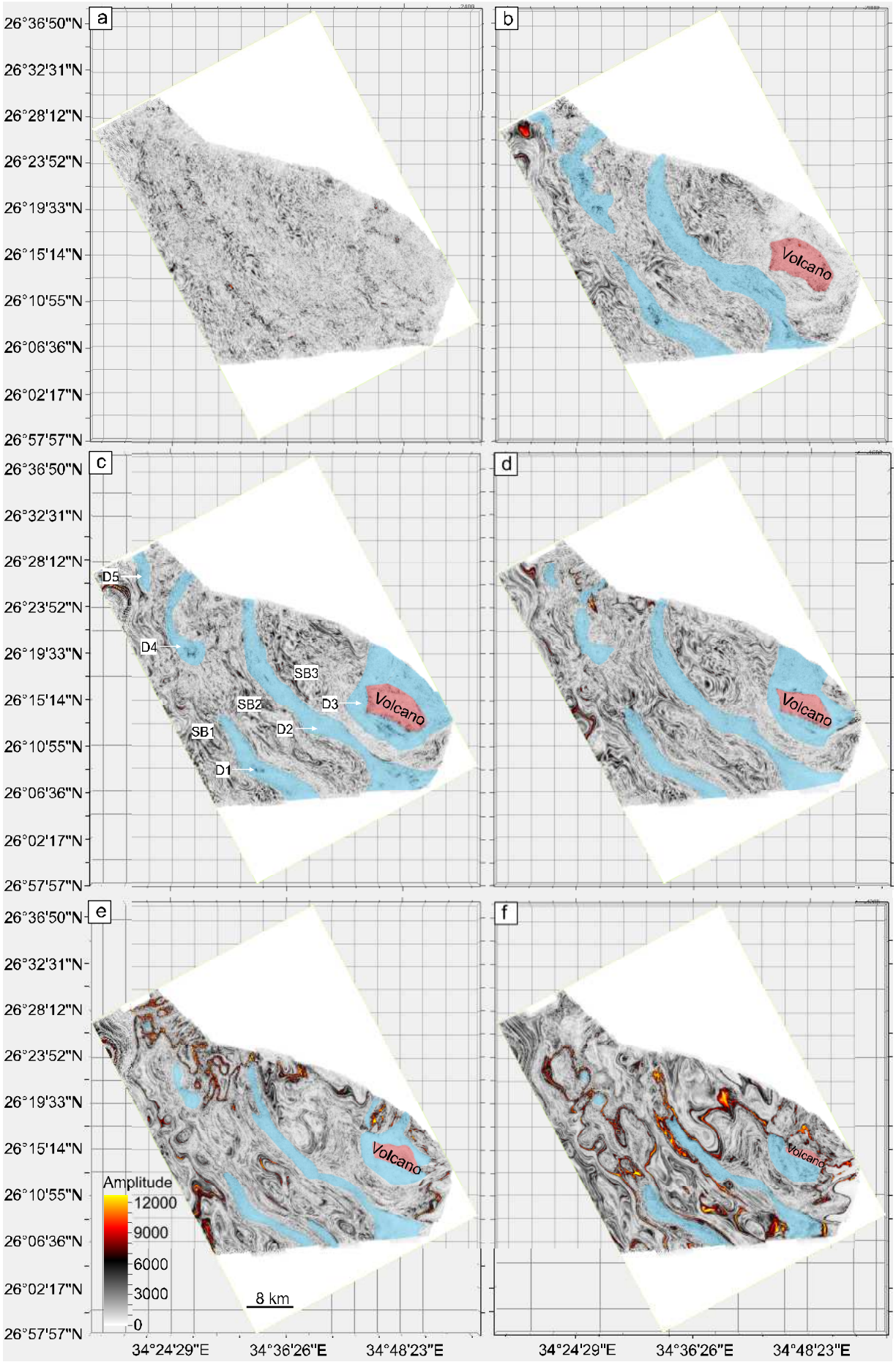

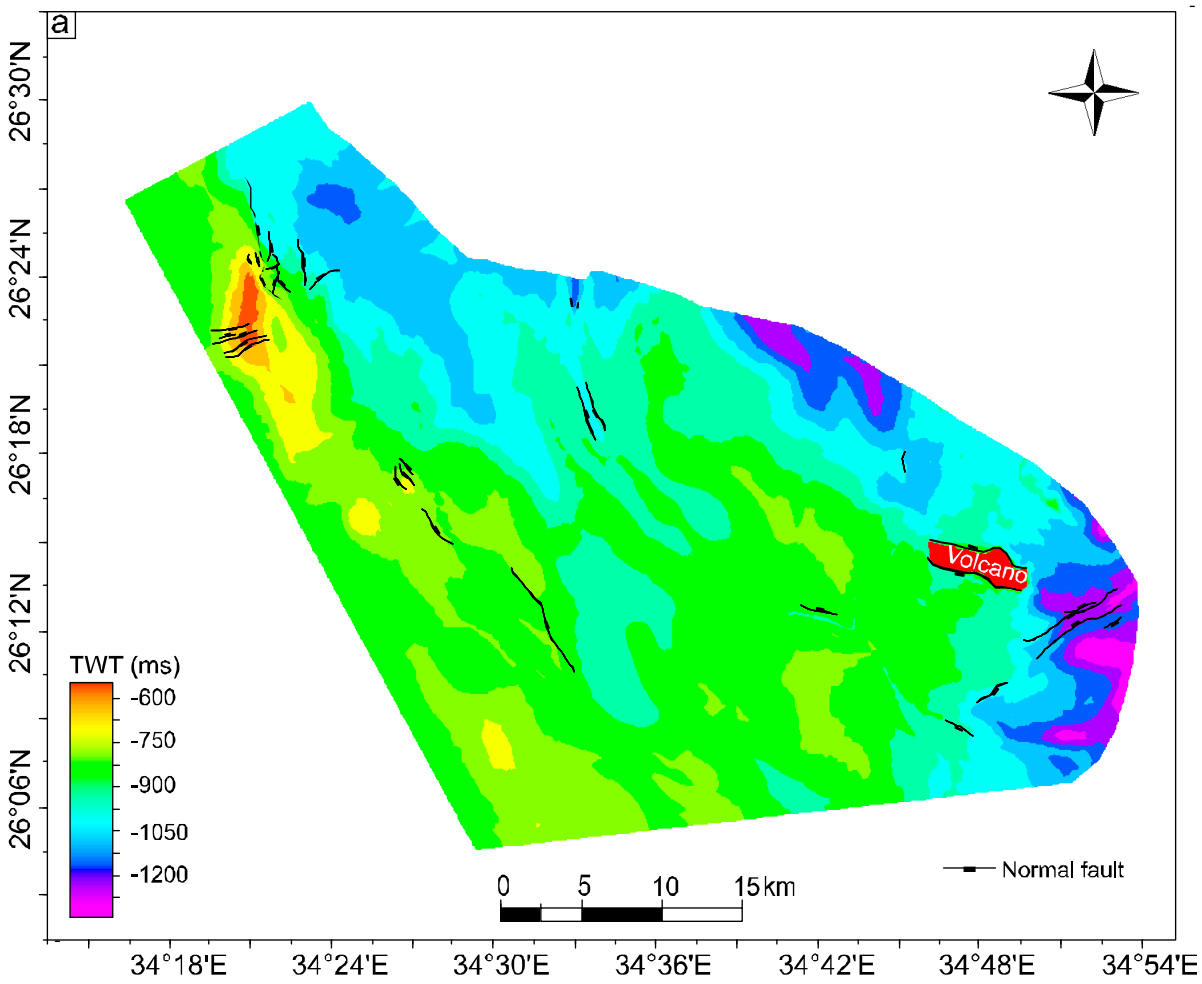

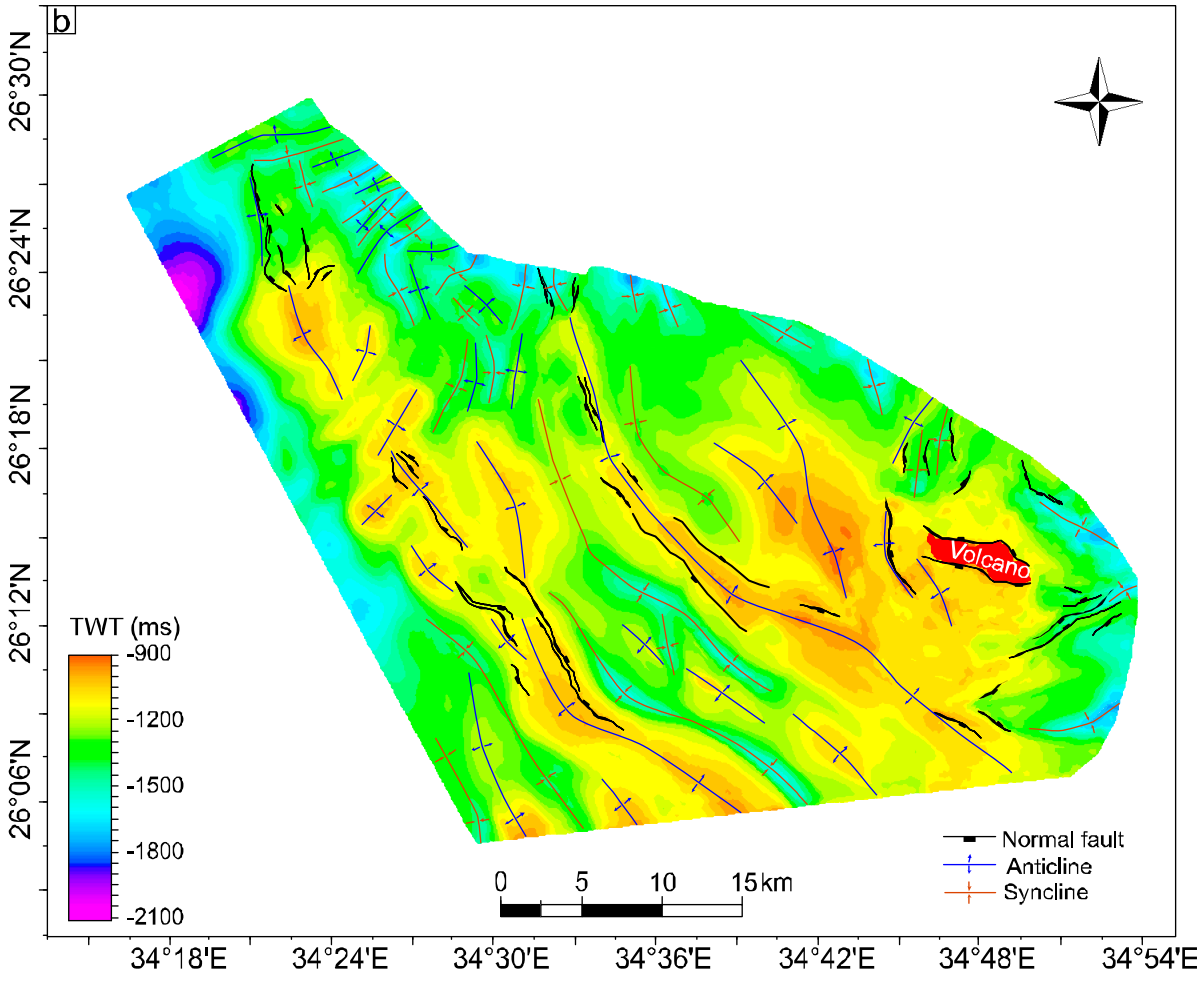

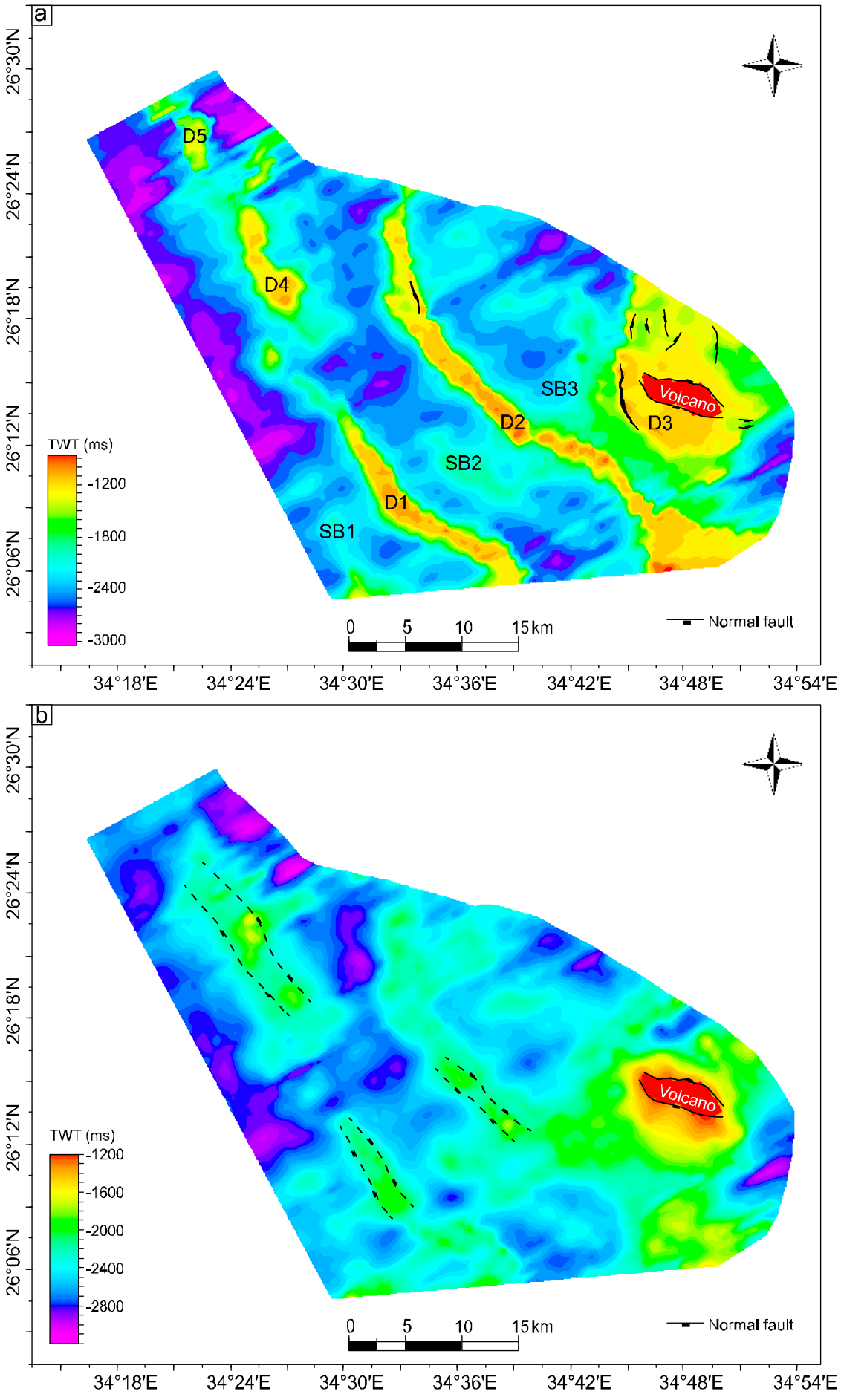

Figure 19

Click here to access/download;Figure;Figure 19.pdf

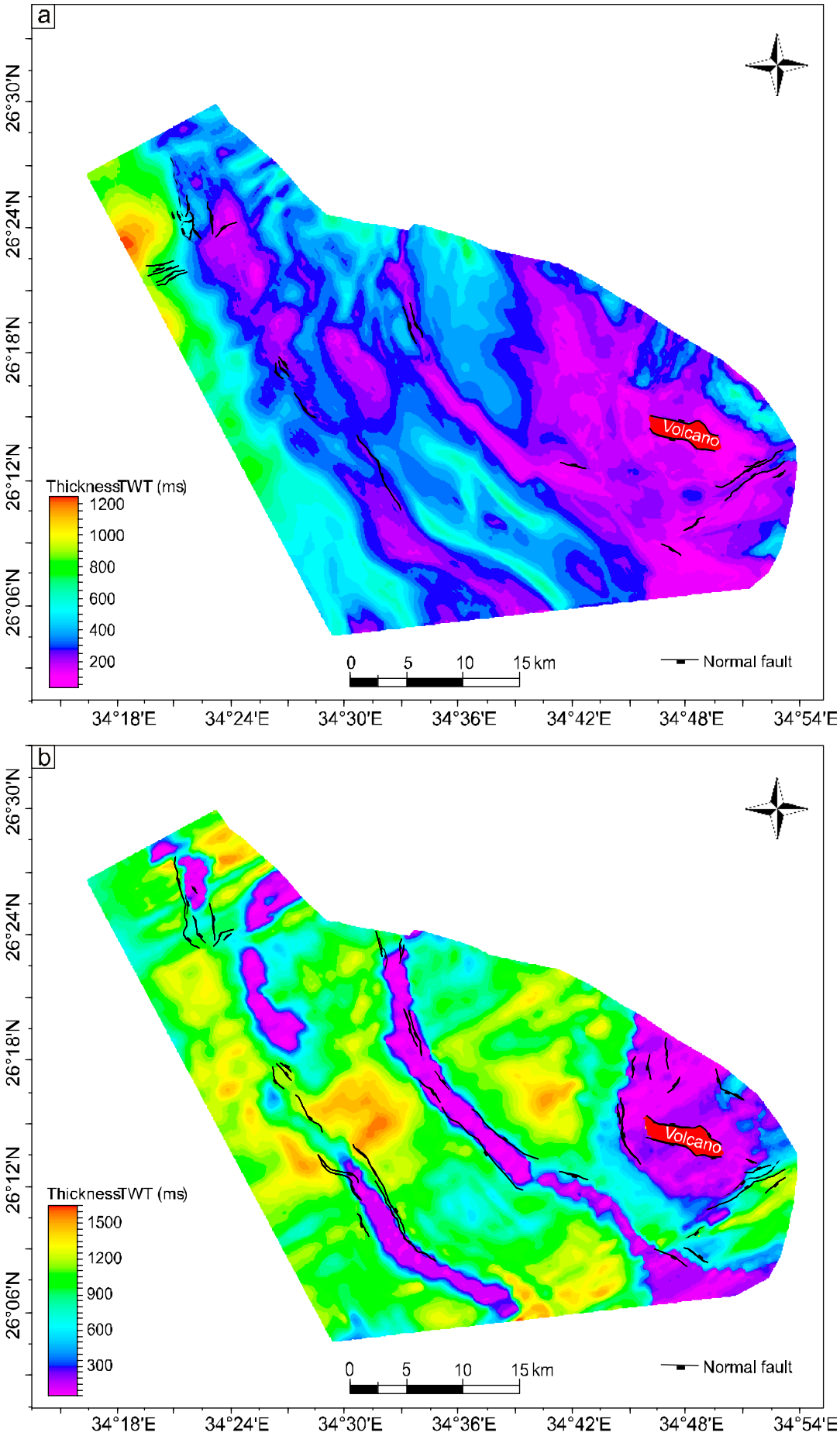

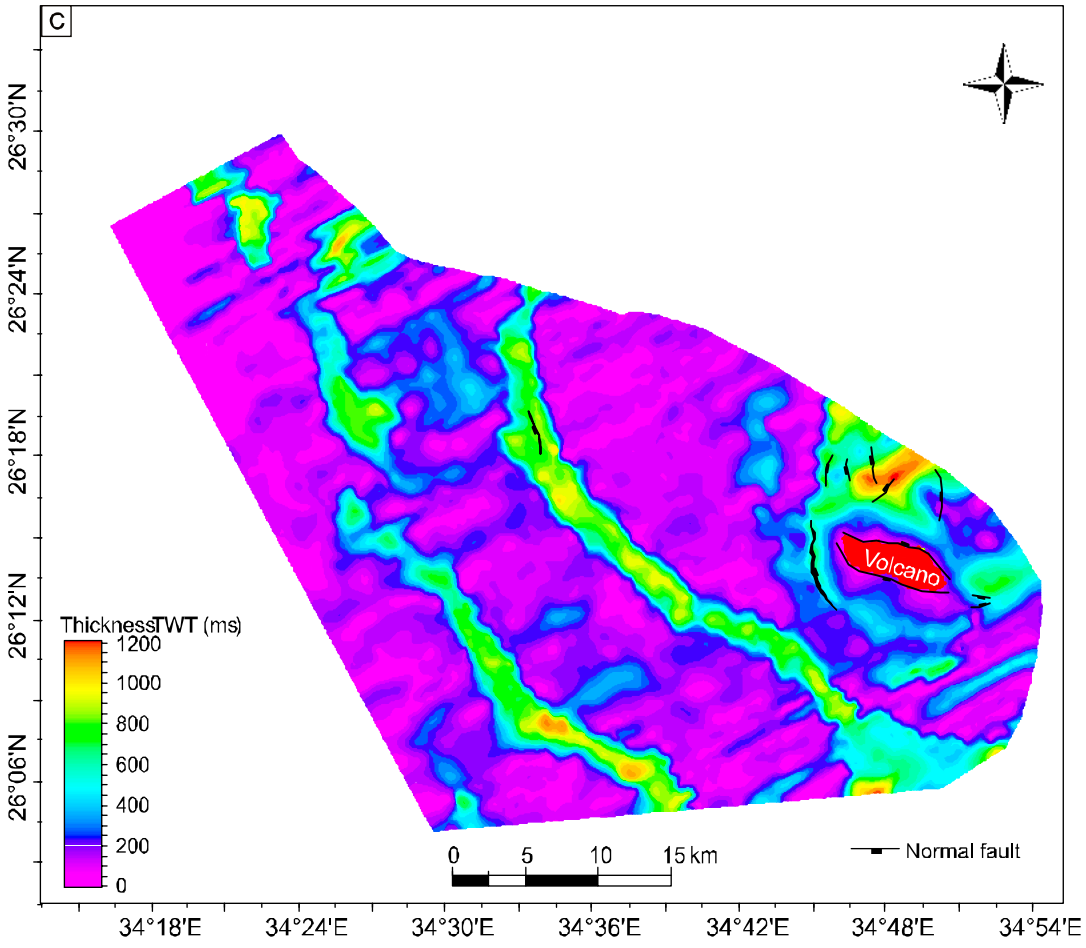
C
26°30'N
26°24'N
26°18'N
26°12'N
26°06'N
34°18'E
34°24'E
34°30'E
34°36'E
34°42'E
34°48'E
34°54'E
Volcano
ThicknessTWT (ms)
1200
1000
800
600
400
200
0
0
5
10
15 km
Normal fault

Figure 20

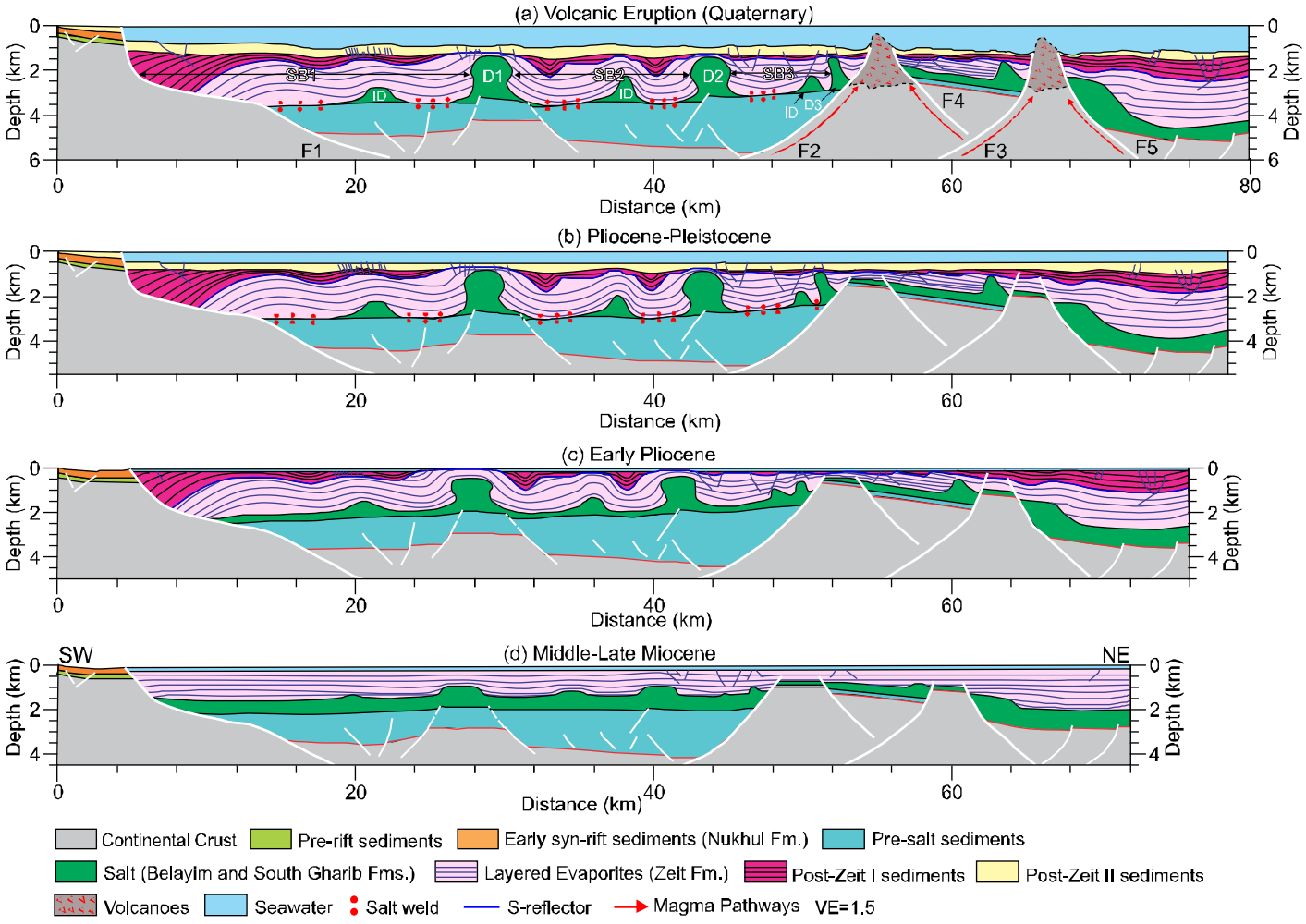

Table 1. The average velocity of the available units in the NRS (Gaulier et al., 1988; Makris and Rihm, 1991; Rihm et al., 1991; Saleh et al., 2006; Ligi et al., 2018).

Unit Name	Average Velocity (m/s)
Seawater	1525
Plio-Quaternary	2000
Layered evaporites	3300
Salt layer	4200
Pre-salt II	2700
Pre-salt I	2800
Basement	3500

Video

Click here to access/download
Supplementary Material
Top Salt.mp4